Final Technical Report

Award number	DE-EE0008532	
Project title	Mitigation of Molten Salt Corrosion	
Recipient organizations	Purdue University	
Principal investigator	Kenneth H. Sandhage Reilly Professor of Materials Engineering E-mail: sandhage@purdue.edu Phone number: +1 765-496-8109	
Business contact	Suzanne Payne Office of Sponsored Program Services Email: shpayne@purdue.edu; spsdoe@purdue.edu Phone number: +1 765-494-6204	
Technology manager	Levi Irwin	
Project officer	Christine Bing	
Contracting officer	Diana Bobo	
Project period	**Start**: 02/01/19	**End**: 1/31/21 (with 6 month no-cost extension)

Acknowledgement: This material is based upon work supported by the Department of Energy, Office of Energy Efficiency and Renewable Energy, Solar Energy Technologies Office, under Award Number DE-EE0008532.

EXECUTIVE SUMMARY

The desire to increase the peak operational temperature of Concentrated Solar Power (CSP) plants to lower the levelized cost of CSP-derived electricity [1-4], has led to consideration of an earth-abundant, low-cost, thermally-stable, molten $MgCl_2$-KCl-NaCl (40-40-20 mole%) salt for high-temperature thermal energy storage and heat transfer [5-7]. The reliable, long-term containment of such a molten salt is challenging, however, due to the corrosion of cost-effective, high-temperature structural metal alloys in this salt (particularly if this salt is contaminated with oxygen-bearing species) [8,9]. This project has been focused on: i) development of equipment for evaluating corrosion kinetics in molten chlorides under well-controlled thermal, fluid dynamic, and atmospheric conditions at CSP-relevant temperatures, ii) use of such equipment to evaluate the influence of forced convection on corrosion kinetics (to determine the role of liquid phase diffusion on such corrosion), and iii) identifying a corrosion-mitigation strategy that can be industrially applied to achieve a projected annual corrosion $\leq$30 μm at CSP-relevant temperatures.

The overall goals of this project have been: i) to understand the rate-limiting step(s) and associated kinetic laws governing corrosion in molten chlorides at 750^{o}C, ii) to determine key operational parameters affecting the corrosion kinetics in molten salts, and iii) to demonstrate the tailoring of such parameters to appreciably reduce such corrosion.

Key accomplishments of this project include:

- *The design and construction of a rotating-disk corrosion testing apparatus capable of evaluating corrosion kinetics in molten chlorides under well-controlled thermal, atmospheric, and fluid dynamic (forced-convective) conditions*
  - The rotating-disk corrosion testing apparatus has been operated at 750^{o}C in a dry flowing Ar atmosphere with an oxygen partial pressure $\leq 10^{-14}$ atm at rotation rates from 50 rpm to 1000 rpm in a molten $MgCl_2$-KCl-NaCl (40-40-20 mole%) salt.
- *Evaluation of the influence of molten salt flow on the corrosion of a Ni-based alloy*
  - The mass change per area, and the surface Cr-Al depletion zone thickness, of Haynes 214 (a Ni-Cr-Al-Fe-based alloy) specimens were not found to increase as the specimen rotation rate increased in a $MgCl_2$-KCl-NaCl liquid bath at 750^{o}C at a low oxygen partial pressure ($\leq 10^{-14}$ atm). Although appreciable scatter was observed in this data, these results were inconsistent with liquid-phase diffusion as a rate-limiting step for H214 corrosion in molten $MgCl_2$-KCl-NaCl under these conditions.
- *Identification of oxidation-resistant molten chlorides and demonstration of such chloride stability in ambient (water-vapor-bearing) air at 750^{o}C, along with a corrosion mitigation strategy for containing such liquids*
  - Thermodynamic calculations indicated that non-$MgCl_2$-bearing molten salts containing $CaCl_2$, $SrCl_2$, $BaCl_2$, NaCl, and/or KCl should be appreciably more oxidation resistant than $MgCl_2$-bearing liquids. These calculations were validated by demonstrating the oxidation resistance of a $CaCl_2$-NaCl (53-47 mole%) eutectic salt in ambient (water-vapor-bearing) air at 750^{o}C (from X-ray diffraction and mass change analyses). NiO-bearing Ni was resistant to corrosion in this salt in air at 750^{o}C, with a slow parabolic weight gain corresponding to a projected annual Ni recession of 14 μm. These strategies may be extended to lower-melting, air-stable chlorides (e.g., $CaCl_2$-NaCl-$BaCl_2$-KCl salts) and to Al_2O_3- or Cr_2O_3-forming alloys.

TABLE OF CONTENTS

SECTION **PAGE**

LIST OF FIGURES

FIGURE: CAPTION **PAGE**

LIST OF FIGURES (Continued)

FIGURE: CAPTION **PAGE**

LIST OF FIGURES (Continued)

FIGURE: CAPTION **PAGE**

LIST OF FIGURES (Continued)

FIGURE: CAPTION **PAGE**

LIST OF TABLES

TABLE: CAPTION **PAGE**

BACKGROUND

Concentrated solar power (CSP) technology with thermal energy storage (TES) has the potential to facilitate large-scale penetration of renewable solar energy into the electricity grid [1-3], with an associated appreciable reduction in man-made greenhouse gas emissions. Indeed, one of the main competitive attributes of CSP plants is that heat from sunlight can be readily transferred to, and retained in, thermal energy storage (TES) media, such as molten salts, to allow for rapidly dispatchable power and/or continuous power [4]. Molten nitrate salts, such as a non-eutectic salt mixture comprised of 60 wt% sodium nitrate and 40 wt% potassium nitrate (known as "solar salt"), have commonly been used for heat transfer and TES media in CSP installations [10]. However, such nitrate salts are limited in use to temperatures <600^{o}C owing to thermal decomposition into nitrites [10,11]. The drive to raise the inlet temperatures of CSP turbines, for enhanced thermal-to-electrical conversion efficiency [4], has led to consideration of relatively low-cost, earth-abundant molten chloride salts (e.g., $MgCl_2$-KCl-based compositions) as candidates for heat transfer fluids and TES media for next generation CSP plants [5-7]. Unfortunately, such $MgCl_2$-bearing liquids are prone to reaction and contamination with oxygen-bearing species upon high-temperature exposure to ambient air, with associated undesired changes in the composition and properties of the liquid, as well as in enhanced corrosion of metal alloys used to contain such liquids [8,9]. There is a need to identify and understand the corrosion mechanisms of materials exposed to such earth-abundant molten chloride salts at $\geq$750^{o}C under well-controlled thermal, atmospheric, and fluid dynamic conditions, as well as to develop effective strategies for inhibiting such corrosion.

PROJECT OBJECTIVES

- **Overall Objectives:**
  - To understand the rate-limiting step(s) and associated kinetic laws governing the high-temperature corrosion of metal alloys and ceramic composites in molten salts
  - To determine key operational parameters affecting the corrosion kinetics in molten salts
  - To demonstrate the tailoring of such parameters to appreciably reduce such corrosion
- **Expected Outcomes:**
  - One or more practical strategies for appreciably reducing corrosion in molten chlorides

MILESTONE TABLE

TASK NO.	TASK DESCRIPTION	DATE
Task 1	**Develop Corrosion Testing Equipment and Protocols**	
M1	Demonstrate the capability of measuring corrosion kinetics in molten salts at CSP-relevant temperatures under well-controlled thermal, atmospheric, and fluid dynamic conditions	Q3 (M9)
Task 2	**Determine Kinetic Mechanisms Controlling Molten Chloride Corrosion**	
M2	Identify the rate laws and associated mechanism(s) (rate-limiting step(s)) for the corrosion of metallic and ceramic composite specimens in molten chloride salts at CSP-relevant temperatures over a range of atmospheric conditions	Q4 (M13)
Task 3	**Minimize Corrosion Kinetics**	
M3	Determine the atmospheric, chemical, and fluid dynamic conditions required to achieve projected annual corrosion of <30 μm/year for metal alloys and ceramic composites in molten chloride salts at CSP-relevant temperatures	Q6 (M18)
Task 4	**Identify Most Acceptable Corrosion Mitigation Conditions**	
M4	Identify atmospheric, chemical, and fluid dynamic conditions most acceptable to the CSP industry for achieving projected annual corrosion rates ≤30 μm/year for metal alloys and ceramic composites in molten chloride salts at targeted temperatures	Q6 (M18)
EOPG	**Successful Completion of all Milestones**	Q6 (M18)

PROJECT RESULTS AND DISCUSSION

Task 1.0: Develop Corrosion Testing Equipment and Protocols

Milestone 1: Demonstrate the capability of measuring corrosion kinetics in molten salts at CSP-relevant temperatures under well-controlled thermal, atmospheric, and fluid dynamic conditions

Subtask 1.1: Rotating-Disk Corrosion Tests

Subtask status: Successfully accomplished.

A rotating-disk corrosion testing apparatus was designed so as to enable exposure of solid materials to molten chlorides at 750°C under controlled fluid dynamic, chemical, and atmospheric (low or high oxygen partial pressure) conditions. A schematic illustration of the overall system design is shown in **Figure 1.1-1**. A photograph of the system is shown in **Figure 1.1-2**. The rotating-disk corrosion testing apparatus consisted of:

i) a vertical clamshell tube furnace with a 4-foot-long heated zone

ii) a rotating-disk assembly (motor, coupling, tachometer, specimen fixturing)

iii) a sealed vertical tube assembly (silica tube, endcap, flanges, crucible, crucible support, bellows, jack) and

iv) a rigid steel frame (bolted to the lab floor) supporting the rotating-disk assembly and the vertical tube assembly.

A controlled atmosphere was achieved within the vertical tube assembly by use of ISO compression vacuum flanges (endcaps) at the top and bottom of the furnace tube. The top endcap contained a gas-tight, solid-shaft, ferromagnetic fluid, rotary feedthrough (**Figure 1.1-3**). The vertical tube consisted of a 4.33 inch/11.0 cm outer diameter (4.13 inch/10.5 cm inner diameter) transparent silica tube, to allow for viewing of the alignment and position of the rotating specimen, and of the position of the salt-bearing crucible, prior to closing the clamshell furnace and raising the temperature of the furnace. A low-oxygen-partial-pressure, dry Ar atmosphere within the vertical tube assembly was achieved by passing high-purity Ar from a tank through an oxygen-gettering system (i.e., a system utilizing heated titanium as an oxygen getter) and a drierite/ascarite column (to remove water vapor) prior to entry into the vertical tube through a port in the upper endcap (**Figure 1.1-3**). The oxygen partial pressure of the gas atmosphere within the vertical tube system was monitored with an oxygen sensor.

The rotation rate of the sample was controlled over the range of 50-1000 rpm using a variable frequency drive (VFD) connected to an electric motor. The rotation rate was monitored by use of an optical tachometer. The temperature profile of the furnace was measured with a reference thermocouple. The molten salt-bearing crucible, the sample, and a reference thermocouple were positioned within the uniform temperature zone of this vertical tube furnace system during any given corrosion experiment. The signal outputs of the reference thermocouple, oxygen sensor, and tachometer were continuously logged during the course of each experiment.

Photographs of the motor, the magnetic coupling device, the rotating rod, and the endcap at the top of the rotating-disk corrosion testing apparatus are shown in **Figure 1.1-3**. The variable frequency drive (VFD) controlled electric motor is shown as

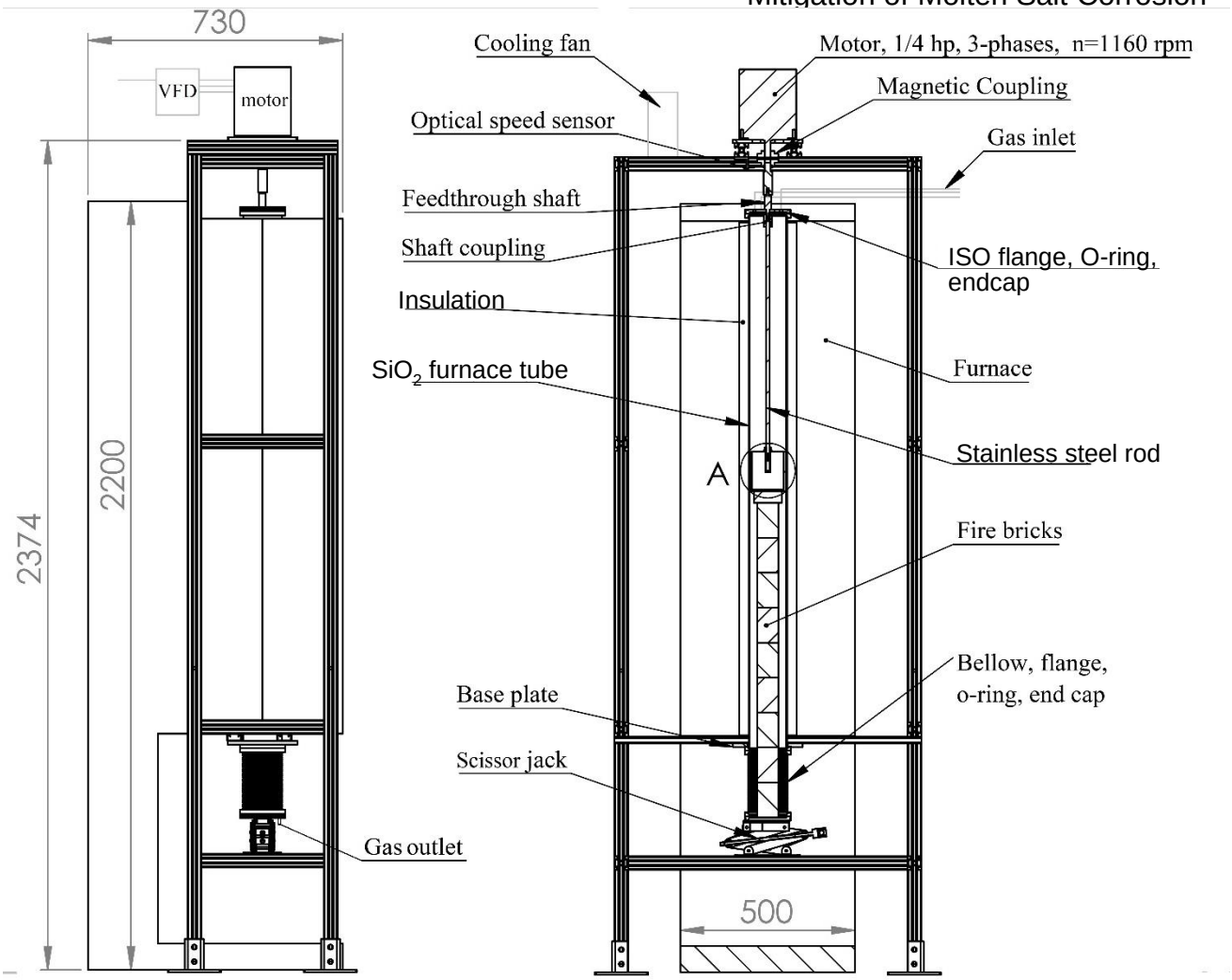

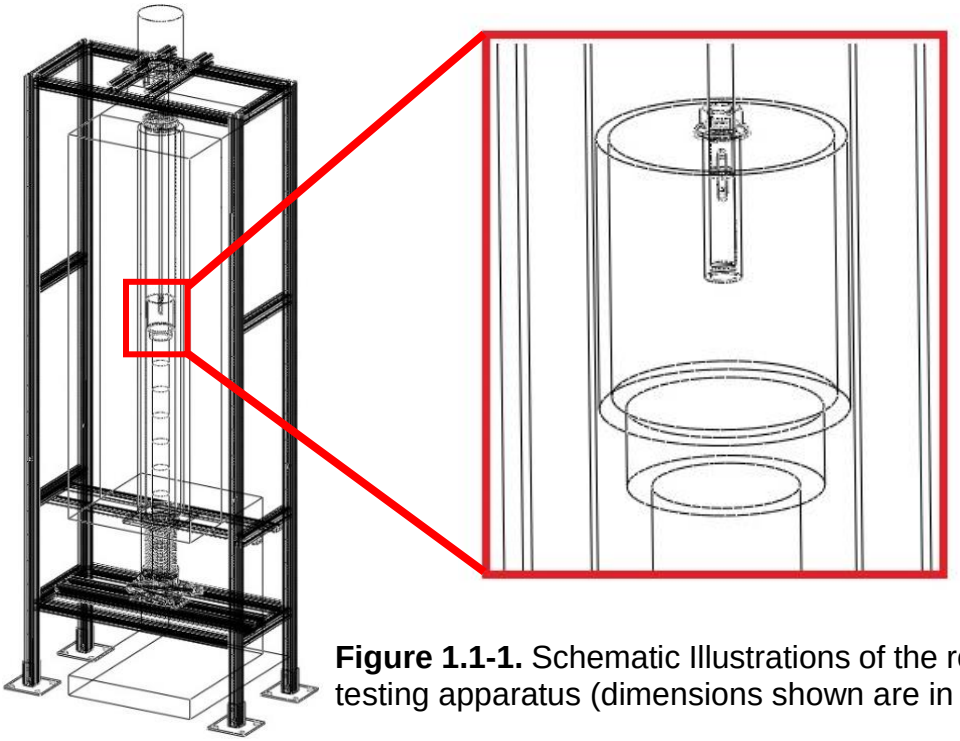

Sample fixturing (see **Fig. 1.1-5** for more details)

Figure 1.1-1. Schematic Illustrations of the rotating-disk corrosion testing apparatus (dimensions shown are in units of mm)

Figure 1.1-2. Photographs of the rotating-disk apparatus revealing components: **A** = motor, **B** = steel support frame, **C** = clamshell vertical (electrically-heated) tube furnace, **D** = furnace controller, **E** = compressible bellows, and **F** = scissor lift jack

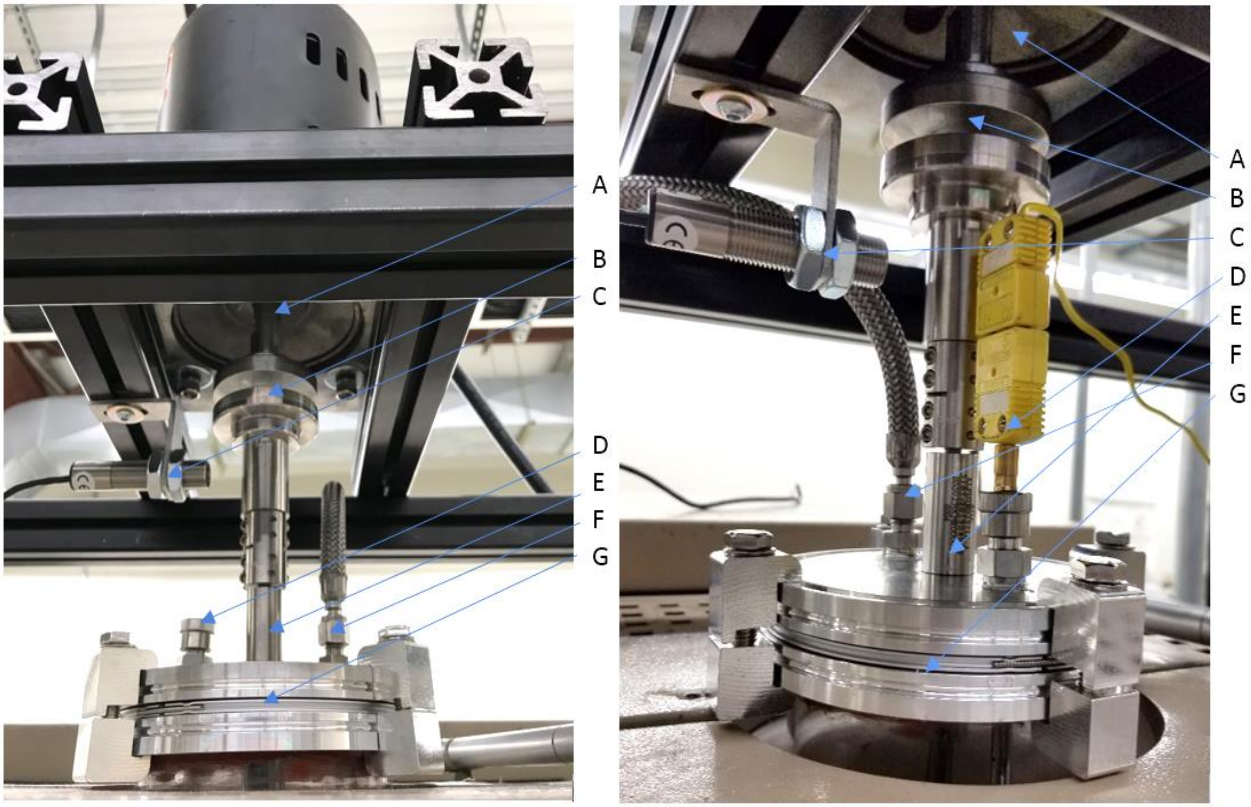

Figure 1.1-3. Photographs of the top assembly of the rotating-disk corrosion apparatus revealing components: **A** = motor, **B** = magnetic coupling disks, **C** = optical tachometer, **D** = thermocouple port, **E** = ferromagnetic fluid feedthrough, **F** = gas inlet port, and **G** = ISO compression endcap sealed to the silica (glass) tube

component A. This motor was coupled to the rotating rod via a magnetic device (component B) consisting of two rare-earth-magnet-based disks separated by a gap of 5 mm. This type of coupling allowed for the transfer of torque from the motor to the spinning rod without transferring vibrations from the motor to the rod. The motor could be unbolted and slid horizontally along the support frame, so as to be placed in a position that would not obstruct the introduction of the rotating rod and sample assembly through the endcap and into silica furnace tube. The motor could then be slid back into position to allow for coupling with the rod during the corrosion test. The rotating rod was connected to the top endcap of the reaction tube (component G) through a gas-tight ferromagnetic fluid feedthrough (component E). The rod rotation was monitored continuously by use of the optical tachometer (component C). A k-type thermocouple was provided through an O-ring-sealed feedthrough port (component D). The desired gas (either oxygen-gettered Ar for a low oxygen partial pressure, or synthetic air for a high oxygen partial pressure) was supplied through the gas inlet port (component F) shown in the top endcap.

A photograph obtained near the mid-height position of the rotating-disk corrosion testing apparatus is shown in **Figure 1.1-4**. The transparent silica (glass) tube (component A) is shown inside the open clamshell furnace (component E). The rotating rod (component B) possessed a threaded bottom to connect to the sample holder (not shown here - see **Figure 1.1-5**). The salt-bearing crucible (component C) was supported

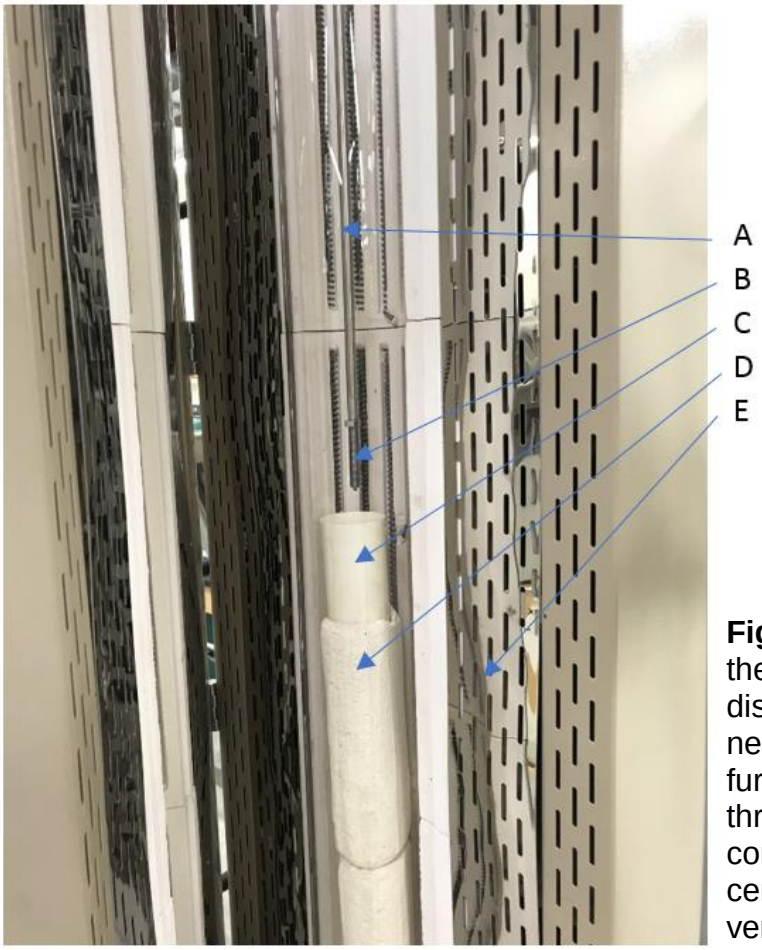

Figure 1.1-4. Photograph obtained at the mid-height location of the rotating disk apparatus revealing components: **A** = transparent SiO_2 (glass) furnace tube, **B** = rotating rod with a threaded bottom, **C** = crucible for containing the molten salt, **D** = ceramic support bricks, **E** = open vertical clamshell tube furnace

by ceramic refractory bricks (component D). At the start (or end) of a test, the crucible was raised (or lowered) using a jack (**Figures 1.1-1, 1.1-2, 1.1-7**) so as to immerse (or remove) the bottom face of the rotating sample into (or out of) the molten salt. Schematic illustrations of the sample holder assembly are shown in **Figure 1.1-5**. A dove-tail groove was machined into each disk-shaped sample. Prior to a corrosion experiment, the sample would be slid into the bottom of a cylindrical sample holder with a mating dove-tail extension. The top of the cylindrical sample holder was connected to the rod with a threaded set screw. The outer sleeve was screwed around the rod. The bottom of the outer sleeve surrounded the outside of the sample (shown most clearly in **Figure 1.1-5c**) so as to prevent the sample from sliding off the dove-tail extension of the cylindrical sample holder upon rotation during a corrosion test. Photographs of a disk-shaped stainless steel (SS) sample with a dove-tail groove, a SS sample holder with a dove-tail extension, and a SS sleeve are shown in **Figure 1.1-6**.

For molten salt corrosion tests conducted in $CaCl_2$-NaCl-based molten salts at high-oxygen-partial-pressure atmospheres (synthetic air) at 750^{o}C, the sleeve and sample holder should be comprised of oxidation-resistant materials, such as pre-oxidized nickel (for NiO-saturated $CaCl_2$-NaCl-based melts), alumina or pre-oxidized alumina-forming alloys (for Al_2O_3-saturated $CaCl_2$-NaCl-based melts), or pre-oxidized chromia-forming alloys (for Cr_2O_3-saturated $CaCl_2$-NaCl-based melts). For molten salt corrosion tests

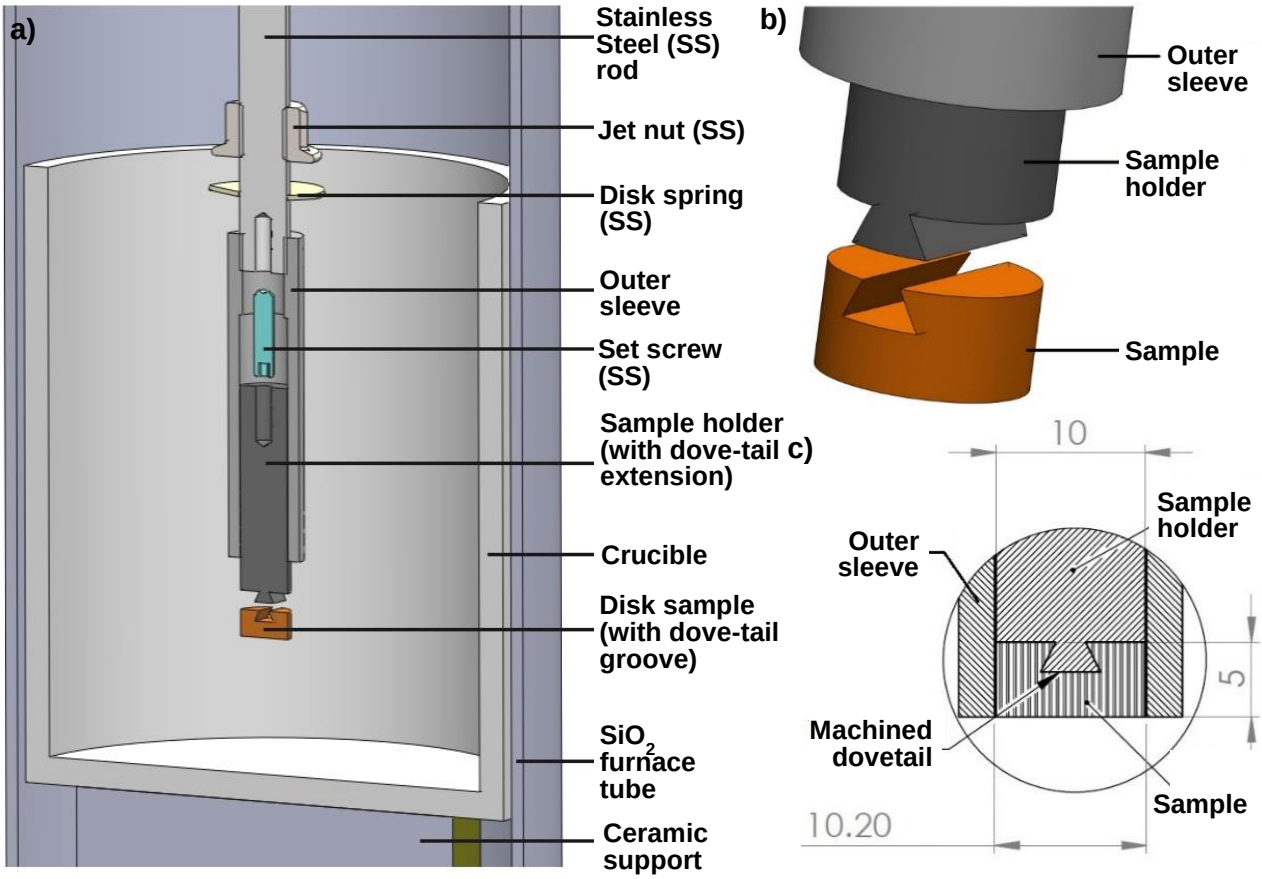

Figure 1.1-5. Illustrations of the sample holder assembly for the rotating-disk apparatus: **a)** overall illustration, **b), c)** higher magnification views of the sample, sample holder, and outer sleeve (dimensions in units of mm)

conducted in low-oxygen-partial pressure atmospheres (oxygen-gettered argon), the sleeve and sample holder may be comprised of graphite. Although graphite is less erosion resistant than metal alloys or ceramics, tests at Purdue have shown that specimens with dovetail grooves can be removed from graphite sample holders (with mating dovetail extensions) with negligible mass change due to graphite deposition onto the specimens.

A photograph of the bottom of the rotating-disk corrosion apparatus is shown in **Figure 1.1-7**. To allow for the vertical motion of the molten salt-bearing crucible at the start and end of an experiment, while keeping the furnace tube sealed (particularly for low-oxygen-partial-pressure tests), flexible bellows (component C) were connected to an endcap at the bottom of the

Figure 1.1-6. Photograph of a 316 SS outer sleeve (left), a 316 SS sample holder (with dovetail extension, middle), and a 316 SS sample (with dovetail groove, right)

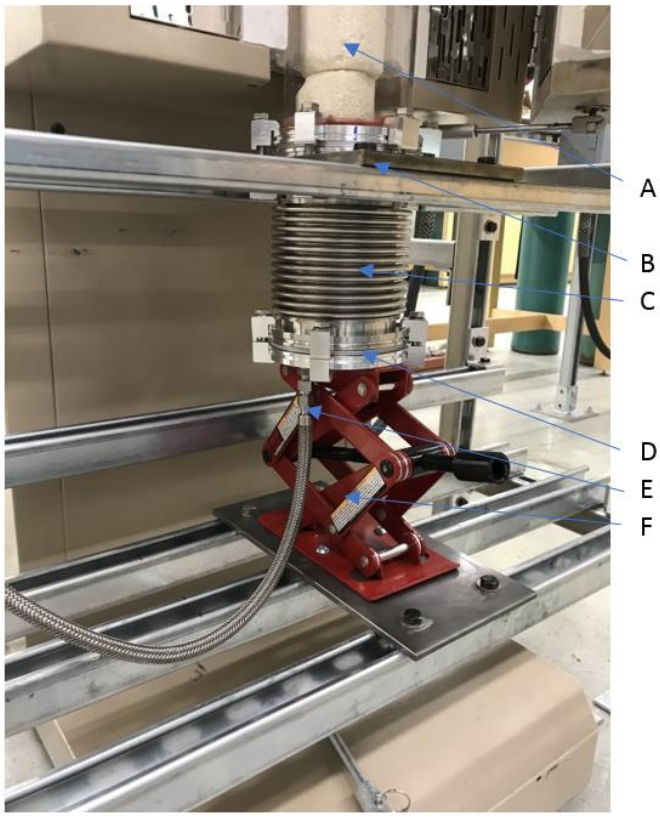

Figure 1.1-7. Photograph of the bottom assembly of the rotating-disk apparatus, revealing the components: **A** = ceramic support bricks, **B** = furnace tube support frame, **C** = compressible bellows, **D** = ISO compression endcap, **E** = gas outlet port, and **F** = scissor jack

silica furnace tube and to an endcap (component D) at the bottom of the bellows. Ceramic refractory bricks (supporting the salt-bearing crucible) were located inside the bellows and the silica furnace tube. A scissor jack (component F) located under the bottom endcap could be raised, so as to compress the bellows and raise the ceramic refractory bricks (and the salt-bearing crucible) without moving the silica furnace tube.

The stationary silica furnace tube was supported by the steel frame (component B). The bottom endcap contained a gas outlet port (component E). The oxygen content of the gas exiting this outlet was monitored with an oxygen sensor (see **Figure 1.1-8**). A photograph of the atmosphere control system, located adjacent to the rotating-disk corrosion testing apparatus, is shown in **Figure 1.1-8**. Once the specimen and salt-bearing crucible were sealed within the silica furnace tube at the start of a low-oxygen-partial-pressure experiment, the air inside the sealed tube was evacuated using a vacuum pump (component F) followed by backfilling with Ar. After conducting such evacuation and backfilling several times, a steady-state Ar flow was passed into (through the gas inlet port in the endcap at the top of the tube) and out of (through the gas outlet port in the bottom endcap) the tube. During such steady-state flow, the Ar entering into the furnace tube was scrubbed of oxygen using the oxygen-gettering (heated Ti) system (component D) and was scrubbed of water vapor using a drierite/ascarite column. The oxygen partial pressure of the Ar exiting the furnace tube was monitored with an oxygen sensor (also in component D). Once a desired low oxygen partial pressure was achieved, the rotation of the specimen commenced and the furnace was heated to 750^{o}C to start the corrosion test. The data logging system (for the oxygen sensor, reference thermocouple, and tachometer) and variable frequency drive (for the electric motor) are also shown (component C) in **Figure 1.1-8**.

Initial testing in this system revealed that the temperature at the top endcap exceeded the allowable range for operation of the ferromagnetic fluid feedthrough (i.e., <80^{o}C). The rotating-disk apparatus was then modified in order to be able to maintain lower temperatures, both at the top and the bottom of the silica tube. A segmented insulative structure was designed and built to minimize heat flow upwards while supporting the

Figure 1.1-8. Photograph of the atmosphere control system adjacent to the rotating-disk corrosion testing apparatus, revealing the components: **A** = motor, **B** = vertical tube furnace, **C** = data logging system and variable frequency drive (VFD) system, **D** = oxygen-gettering system and oxygen sensor, **E** = Ar gas tank, and **F** = vacuum pump

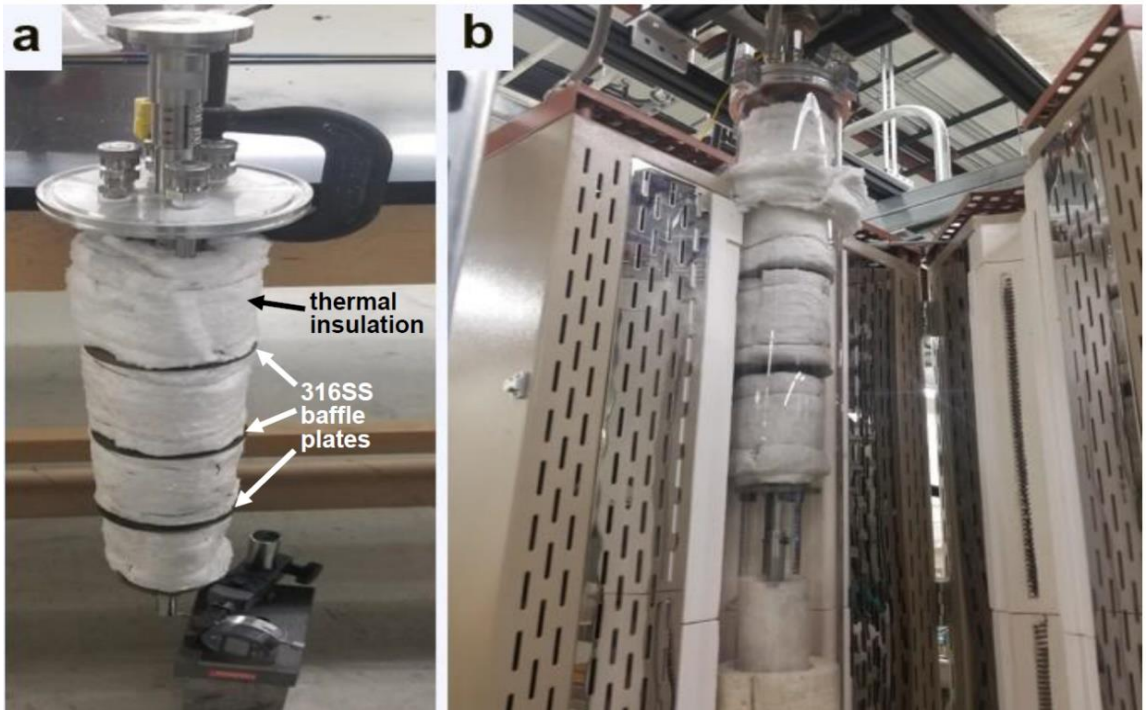

Figure 1.1-9. Photographs of the modified (thermally-insulated) top assembly of the rotating-disk apparatus: **a)** before and **b)** after installation in the furnace

rotating rod via a bottom bushing and allowing for introduction of a reference thermocouple (**Figures 1.1-9a and b**). The gas flow into the tube was also modified, as shown in **Figure 1.1-10**, to allow for active cooling of the rotating rod. After these modifications, the temperature at the ferromagnetic fluid feedthrough during operation of the furnace at 750^{o}C was reduced to 30^{o}C (i.e., well within the allowable range of operation for this ferromagnetic fluid).

It was also discovered that the bottom flanges, endcaps, and flexible bellows were prone to excessive corrosion from vapor gas species generated during purification of the molten $MgCl_2$-NaCl-KCl salt in this system. Indeed, atmosphere control was lost due to a complete corrosive breach of the flexible bellows (**Figures 1.1-11** and **1.1-12**).

Figure 1.1-10. Photograph of the modified top assembly, with the blue arrow depicting redirection of inlet gas flow for active cooling

Figure 1.1-11. Excessive corrosion of the bottom stainless steel bellows, after exposure for 12 h to Ar gas passed over non-purified $MgCl_2$-KCl-bearing salt at 750^{o}C

Figure 1.1-12. Corrosion of the Al bottom flange after exposure for 2 h to Ar that had been passed over non-purified $MgCl_2$-KCl-bearing salt for 2 h at 750^{o}C

To avoid such excessive corrosion, a separate dedicated ceramic tube furnace was then used for molten chloride salt purification (via thermal treatment in a low-oxygen, low-

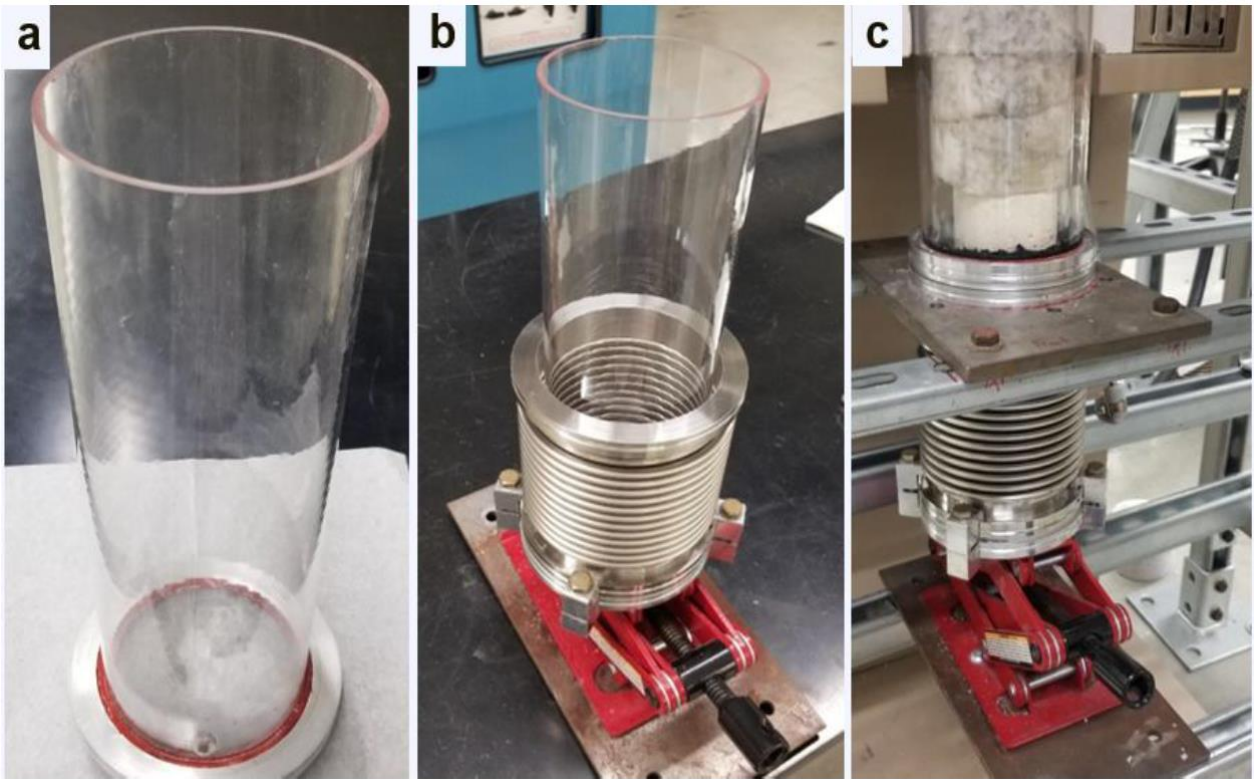

Figure 1.1-13. Photographs of the modified bottom assembly of the rotating-disk testing apparatus: **a)** bottom endcap with a silica inner tube fixed in place with RTV (silicone rubber adhesive), **b)** assembly with the liner in place, and **c)** with the thermal insulation

Figure 1.1-14. Photographs of the inspected bottom bellows after exposure to Ar gas passed over $MgCl_2$-KCl-bearing salt at 750°C for 6 h

water Ar atmosphere). An inner glass liner and thermal insulation were also added to the corrosion experiment (**Figure 1.1-13**). The bottom bellows, after use in a 6 h experiment with $MgCl_2$-KCl-NaCl salt at 750°C for 6 h, is shown in **Figure 1.1-14**. With these modifications, appreciable corrosion of the lower bellows was avoided.

Preliminary testing at relatively high rotation rates (e.g., 1000 rpm) revealed the need for enhanced support of the upper endcap and furnace tube to avoid lateral movement of the endcap/tube assembly (and excessive wobbling of the rotating rod/specimen assembly). A two-part supporting aluminum plate was designed and fabricated, as shown in **Figure 1.1-15a**. This plate, which contains a central hole lined with four pieces of high-density rubber, was clamped around the upper endcap, as shown in **Figure 1.1-15b**. This

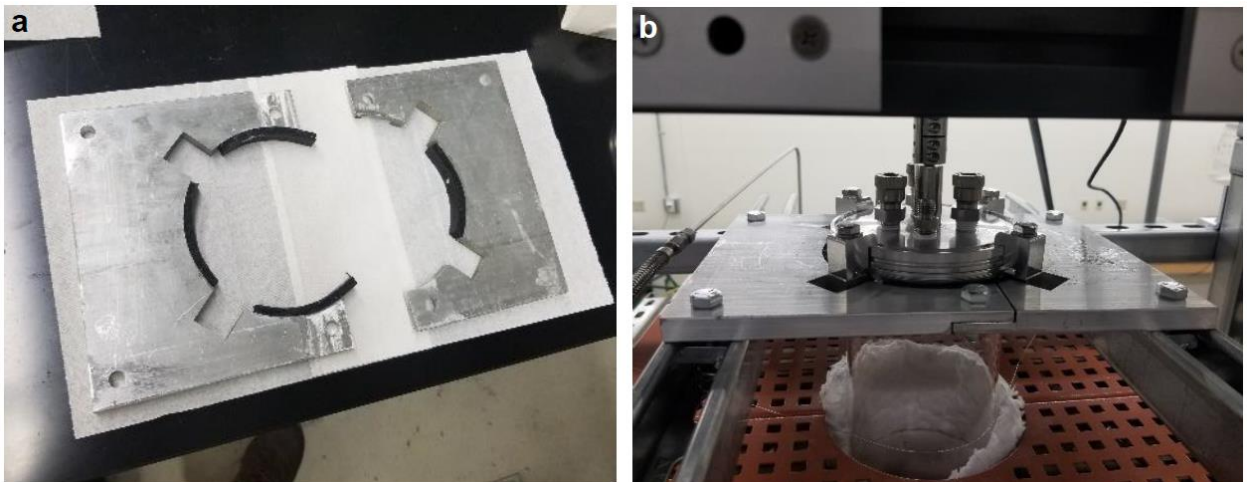

Figure 1.1-15. Modified top assembly of the rotating-disk corrosion testing apparatus to avoid lateral motion of the upper endcap and furnace tube during rotation at high rates

design allowed for thermal expansion of the reaction tube assembly in the vertical direction, while avoiding lateral motion of the endcap and furnace tube (and rotating rod).

The sample holder design was also modified to minimize wobbling of the rotating-disk at high rotation rates. The threaded rod initially used for connection to the rotating rod was replaced by a dove tail extension, as shown in **Figure 1.1-16a**. The sample sleeve, sample holder, and sample, were then vertically fixed by use of a pin and aligned for rotation with three sets of Ni screws (**Figure 1.1-16b**). This arrangement resulted in a reduction of the wobble of the specimen to <0.2 mm. A stainless-steel cover plate was also added to both prevent debris from falling into the test crucible from above, and to constrain the vertical migration of the pin sleeve. Finally, an alumina bushing insert was placed between the rotating rod and the steel bushing to minimize wear of the steel bushing and to avoid seizing of the rotating rod (due to friction welding) with the steel bushing (**Figure 1.1-17**). As a rough commissioning test and **in line with Milestone 1** for the overall rotating-disk corrosion apparatus, a stainless-steel specimen was immersed with rotation (100 rpm) in chloride liquid at 750°C in a low-oxygen ($pO_2 = 10^{-14}$ atm) Ar environment, removed from the melt, cooled to room temperature, and successfully removed from the sample holder via dissolution of the adhering solidified salt in water.

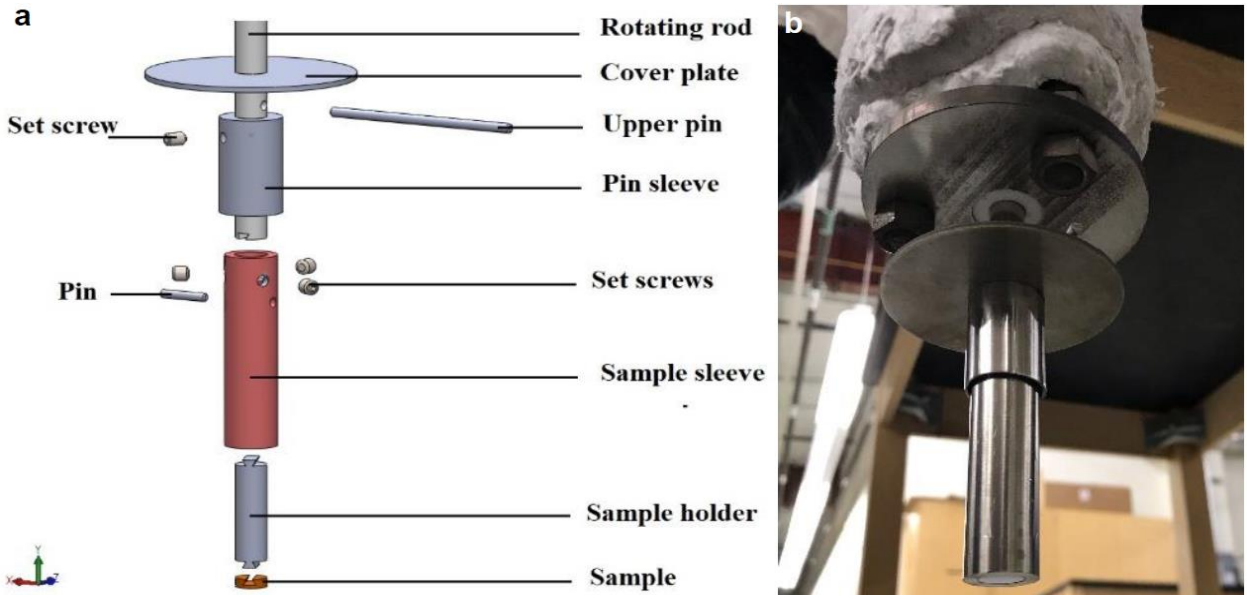

Figure 1.1-16. a) Schematic illustration and **b)** photograph of the modified specimen holder assembly used to minimize wobbling of the rotating specimen at high rotation rates

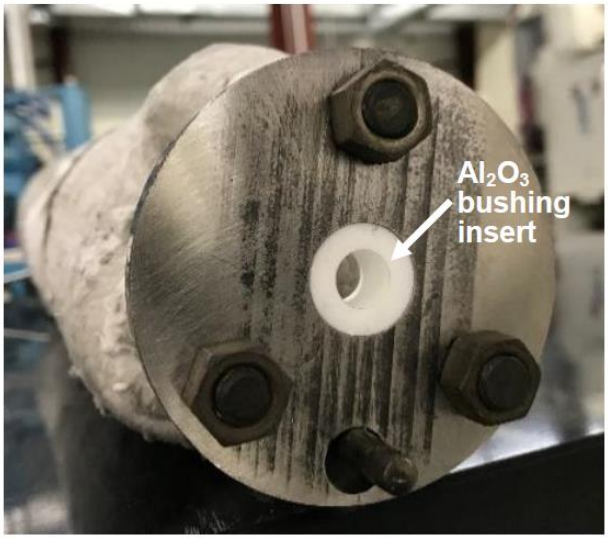

Figure 1.1-17. Photograph of the alumina bushing insert placed between the rotating rod (not shown) and the steel bushing (to minimize wear of the steel bushing and to avoid friction welding of the rotating rod to the steel bushing

Subtask 1.2: Thermogravimetric Corrosion Tests

Due to the delays caused by the 3-month lab shutdown because of COVID19, and the budgetary restrictions imposed by such shutdown, this task was stopped.

Task 2: Determine Kinetic Mechanisms Controlling Molten Chloride Corrosion

Milestone 2: Identify the rate laws and associated mechanism(s) (rate-limiting step(s)) for the corrosion of metallic and ceramic composite specimens in molten chloride salts at CSP-relevant temperatures over a range of atmospheric conditions

Subtask 2.1: Corrosion at Low Oxygen Partial Pressures

Rotating Disk Fluid Dynamics for Laminar Flow in a Semi-Infinite Liquid Bath

For a corrosion process controlled by mass transport (of dissolved species) through a molten salt, the corrosion kinetics can be described by the Noyes-Nernst equation [12]:

$$j_{D,i} = \frac{D}{\delta^*}(C_i - C_b) \quad (1)$$

where $j_{D,i}$ is the flux of the rate-controlling solute species i in the molten salt, D is the diffusion coefficient of solute species i in the molten salt, δ^* is the thickness of the concentration boundary layer in the molten salt, C_i is the concentration of the solute species i at the solid/liquid interface (the saturation concentration of solute species i in the molten salt) and C_b is the concentration of the solute species i in the bulk molten salt. The concentration boundary layer thickness, δ^*, developed at the bottom face of a rotating cylinder is described by the Levich-Cochran equation [13,14]:

$$\delta^* = 1.61\left(\frac{D}{\nu}\right)^{\frac{1}{3}}\left(\frac{\nu}{\omega}\right)^{\frac{1}{2}} \quad (2)$$

where δ^* (cm) is the concentration boundary layer thickness in the molten salt, D (cm^2/s) is the diffusion coefficient of solute species i in the molten salt, ν (cm^2/s) is the kinematic viscosity of the molten salt, and ω (rad/s) is the angular velocity of the rotating specimen. Use of the Levich-Cochran equation requires laminar fluid flow (i.e., a Reynolds number, Re, below $2x10^5$ for flow with a rotating disk) and a bath of semi-infinite size. The Reynolds number is defined as:

$$Re = \frac{r^2\omega}{\nu} \quad (3)$$

where r is the disk radius (0.5 cm). The following physical properties for the ternary salt composition $MgCl_2$-KCl-NaCl (40-40-20 mol%) were used to estimate the Re number and the concentration boundary layer thickness in the molten salt:

- a diffusion coefficient (D) for Cr^{3+} in the ternary $MgCl_2$-KCl-NaCl at 750°C of $2.94x10^{-5}$ cm^2/s (determined by Dr. Jinsuo Zhang of Virginia Tech, currently unpublished).
- a dynamic viscosity of 2.4 cP (0.024 g/cm·s) at 750°C [15]
- a density of 1.578 g/cm^3 at 750°C [15]

Division of the dynamic viscosity by the density yielded a kinematic viscosity value of 1.5 cSt (0.015 cm^2/s) for the molten salt at 750°C. For rotation rates ranging from 50-1000 rpm (5.2-105 rad/s), the Re number values ranged from 87-1750 (well below the Re = $2x10^5$ threshold for a transition to turbulent flow). For a diffusion coefficient value of $2.94x10^{-5}$ cm^2/s, the values of the concentration boundary layer thickness calculated from equation (2) for rotation rates of 50-1000 rpm ranged from 0.011 cm to 0.0024 cm (110-24 µm). These δ^* values were 250-1150 times smaller than the internal radius of the Al_2O_3 crucible (2.75 cm) and 410-1880 times smaller than the depth of the molten salt below the bottom face of the H214 specimens in the crucible (approximately 4.5 cm); that is, the molten $MgCl_2$-KCl-NaCl salt bath was effectively semi-infinite in size (2-3 orders of magnitude larger than the concentration boundary layer thickness).

Hence, the conditions of the rotating-disk corrosion experiments were consistent with laminar flow in a semi-infinite liquid bath which, in turn, allowed for evaluation of the role

of liquid-phase diffusion on the kinetics of corrosion via comparison of experimental data with predictions from equations (1) and (2); that is, if liquid phase diffusion is the rate-limiting step for corrosion of a rotating specimen, then the corrosion rate should increase with an increase in the square root of the specimen rotation rate (i.e., the change in mass per area should be proportional to the diffusion flux which should proportional to the square root of the specimen rotation rate; $\Delta m/A \alpha j_{D,i} \alpha \omega^{1/2}$).

Forced-Convective (Rotating Disk) Corrosion of H214

The rotating-disk apparatus was used to evaluate the corrosion behavior of Haynes 214 (H214, an Al_2O_3-forming Ni-based alloy comprised of 16 wt%/17 at% Cr, 4.5 wt%/9.1 at% Al, 3 wt%/2.9 at% Fe, <2 wt%/1.9 at% Co) in molten $MgCl_2$-KCl-NaCl (40-40-20 mol%) salt at 750°C at low oxygen partial pressures ($pO_2 < 10^{-14}$ atm) and at rotation rates of 50 rpm, 100 rpm, 287 rpm, 433 rpm, 687 rpm, and 1000 rpm. These corrosion tests were conducted with molten $MgCl_2$-KCl-NaCl salt held in Al_2O_3 crucibles (internal dia. = 5.5 cm) and with the H214 samples held in place using fixturing comprised of Al_2O_3.

The $MgCl_2$ (T_m = 714°C), KCl (T_m = 771°C), and NaCl (T_m = 801°C) constituents (all >99.0 wt% purity with respect to inorganic contaminants) were individually pre-melted at 750°C, 800°C, and 850°C, respectively, for 1 h in graphite crucibles under a flowing (1 L/min) oxygen-gettered ($pO_2 \leq 10^{-14}$ atm) dry Ar atmosphere within a controlled-atmosphere tube furnace. These salt constituents were then stored in an Ar-atmosphere glovebox with oxygen and water vapor partial pressures maintained at < 1 ppm. Just prior to a given corrosion test, the individual salt constituents were mixed in appropriate ratios in the glovebox using a mortar and pestle. A $MgCl_2$-KCl-NaCl batch size of 200 g was placed in an Al_2O_3 crucible (>99.6 wt% purity, 5.2 cm internal diameter x 9.4 cm internal height) within the glovebox. The $MgCl_2$-KCl-NaCl-bearing crucible was quickly transferred into a controlled-atmosphere tube furnace, that was then evacuated and backfilled with oxygen-gettered Ar (using 3 evacuation/backfilling cycles). The $MgCl_2$-KCl-NaCl salt was heated to 750°C and held at this temperature for 1 h in the flowing oxygen-gettered, dry Ar to allow for additional equilibration with this low-oxygen, dry atmosphere. After cooling in flowing oxygen-gettered Ar to room temperature, the solidified-salt-bearing crucible was stored in the Ar atmosphere glovebox for the impending corrosion test.

Cylindrical H214 specimens of 1 cm diameter possessing a dovetail groove on one face were cut from a H214 plate via electrodischarge machining. The flat faces (non-grooved) faces of these specimens were polished to a 15 μm surface finish using a series of SiC-bearing polished pads. The polished specimens were cleaned by sonication for 10 min in de-ionized water, then for 10 min in ethanol, and finally for 10 min in acetone, followed by vacuum drying (10 to 30 mTorr) at room temperature for 15 min. The starting weight of a given H214 specimen was measured using an electronic microbalance just prior to a corrosion test. The H214 specimens were held in place during the corrosion tests using Al_2O_3 fixturing. A schematic illustration of the fixturing used to support the H214 specimens during corrosion tests, and photographs of the fixturing components and the assembled fixturing holding the sample, are provided in **Figure 2.1-1**.

After positioning the $MgCl_2$-KCl-NaCl salt-bearing crucible on a supporting ceramic pedestal within the vertical tube furnace system, and after placing the H214 specimen within the alumina fixturing, the furnace system was closed, evacuated (to 10 to 30 mTorr), and backfilled with oxygen-gettered Ar (using three evacuation and backfilling

cycles). The bottom face of the H214 specimen was positioned above the solid $MgCl_2$-KCl-NaCl salt in the alumina crucible, so that this bottom face would become immersed

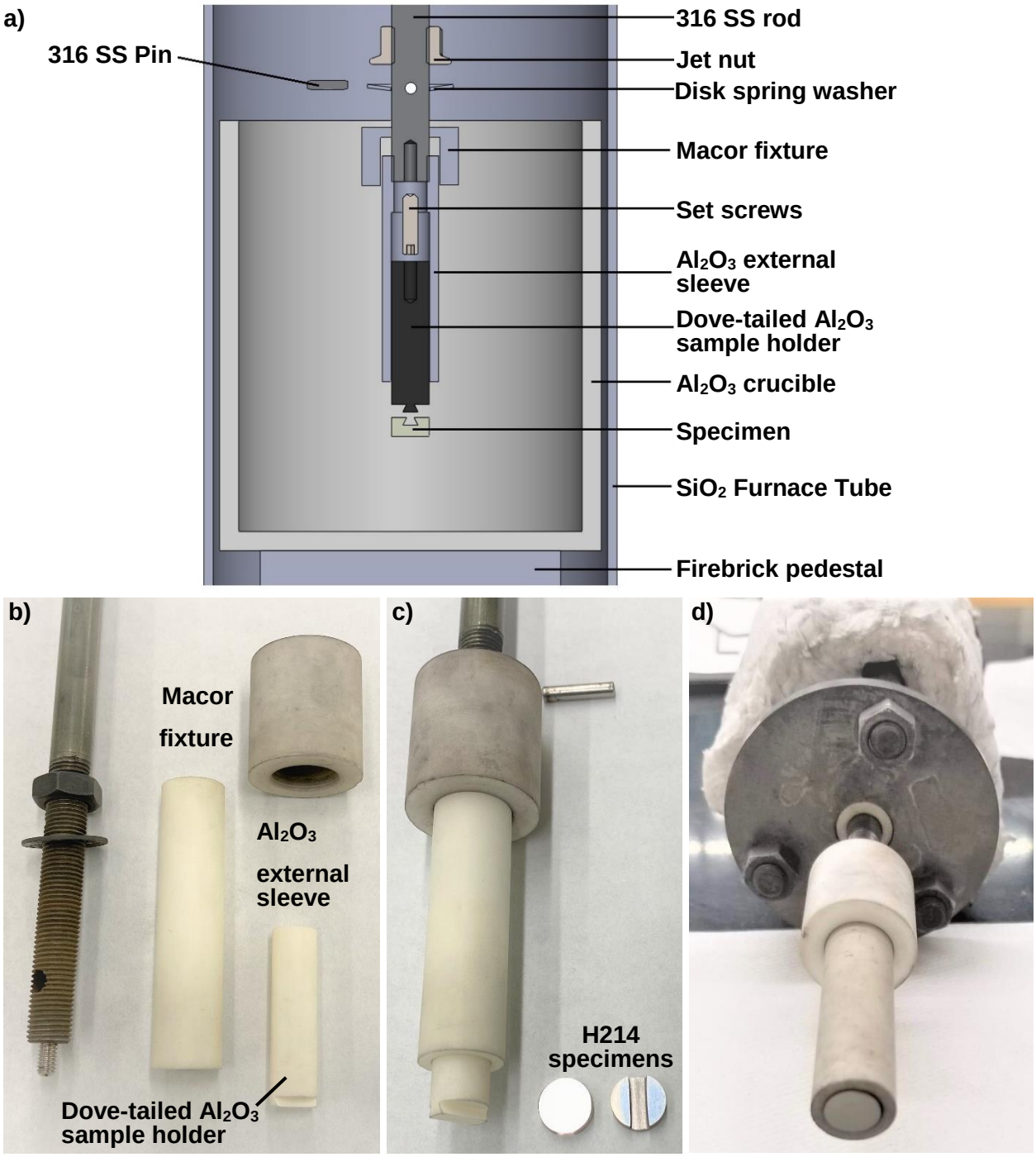

Figure 2.1-1. a) Schematic illustration of the fixturing used to support H214 specimens for corrosion tests, and photographs of: **b)** the disassembled fixturing components used to hold the specimens during the rotating-disk corrosion tests, **c)** the assembled fixturing for holding the specimens and 2 separate polished H214 specimens, and **d)** the assembled fixturing holding a H214 specimen

upon complete melting of this $MgCl_2$-KCl-NaCl salt (i.e., due to the volume expansion upon $MgCl_2$-KCl-NaCl salt melting at about 420°C). After confirming that the oxygen partial pressure of the oxygen-gettered Ar flowing through the furnace system was $<10^{-14}$ atm (using a downstream oxygen sensor), the furnace was heated at 10°C/min to 750°C and then held at this temperature for 1 h (to ensure thermal equilibrium of the specimen with the molten salt bath) prior to starting the specimen rotation. After the desired rotation rate (50±2 rpm, 100±2 rpm, 433±2 rpm, 687±2 rpm or 1000±2 rpm, as measured by an optical tachometer) was achieved (within a few sec), the salt-bearing crucible was raised another 2.0 cm (to further submerge the bottom face of the sample in the molten salt). After 1 h of rotation, the salt-bearing crucible was lowered (so as to remove the specimen from the molten $MgCl_2$-KCl-NaCl salt), the specimen rotation was stopped, and system was cooled at 10°C/min.

The global extent of corrosion of a given sample was determined from the change in specimen mass per exposed surface area. After a corrosion test, the solidified adherent salt was dissolved from the specimen by immersion for 24 h with ultrasonication in de-ionized water at room temperature. The specimen was then immersed with ultrasonication for 10 min in ethanol, and finally for 10 min in acetone, followed by vacuum drying (at 10 to 30 mTorr) at room temperature for 15 min. The weight of each specimen after such salt dissolution was then obtained.

A plot of the mass change per area, $\Delta m/A$, versus the specimen rotation rate, ω, for molten-salt-exposed H214 specimens is shown in **Figure 2.1-2**. A plot of the mass

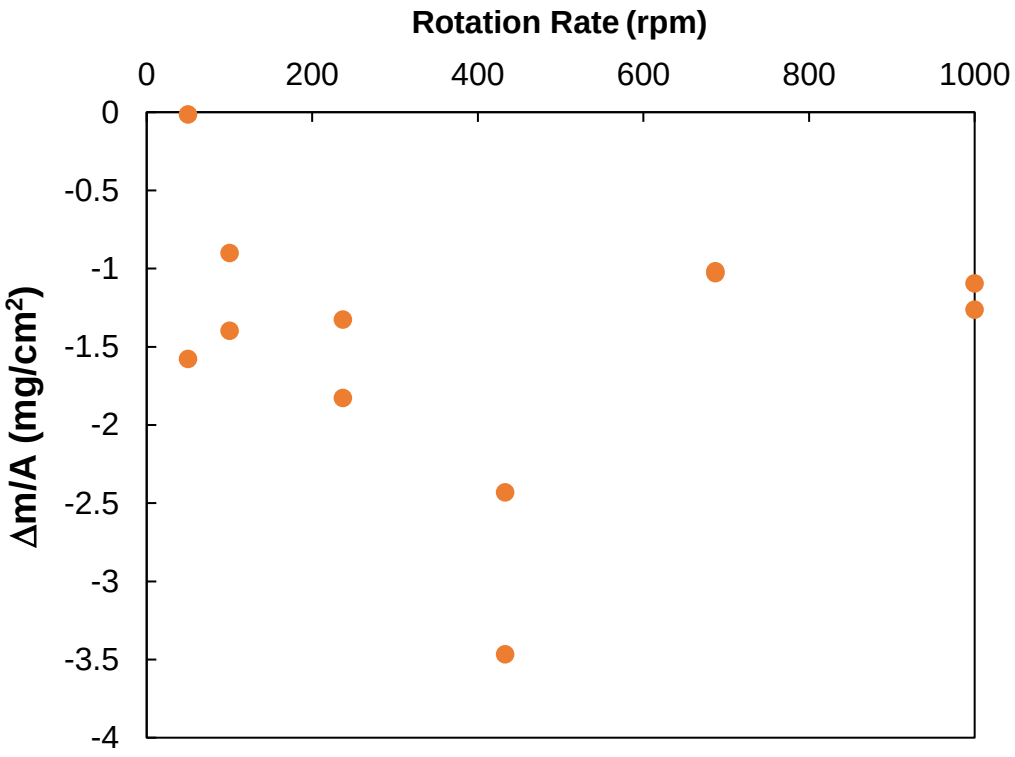

Figure 2.1-2. Plot of the mass change per area, $\Delta m/A$, vs. specimen rotation rate for H214 specimens exposed to molten $MgCl_2$-KCl-NaCl salt at 750°C for 1 h (after dissolution of adhering, solidified molten salt from the specimens via exposure to water)

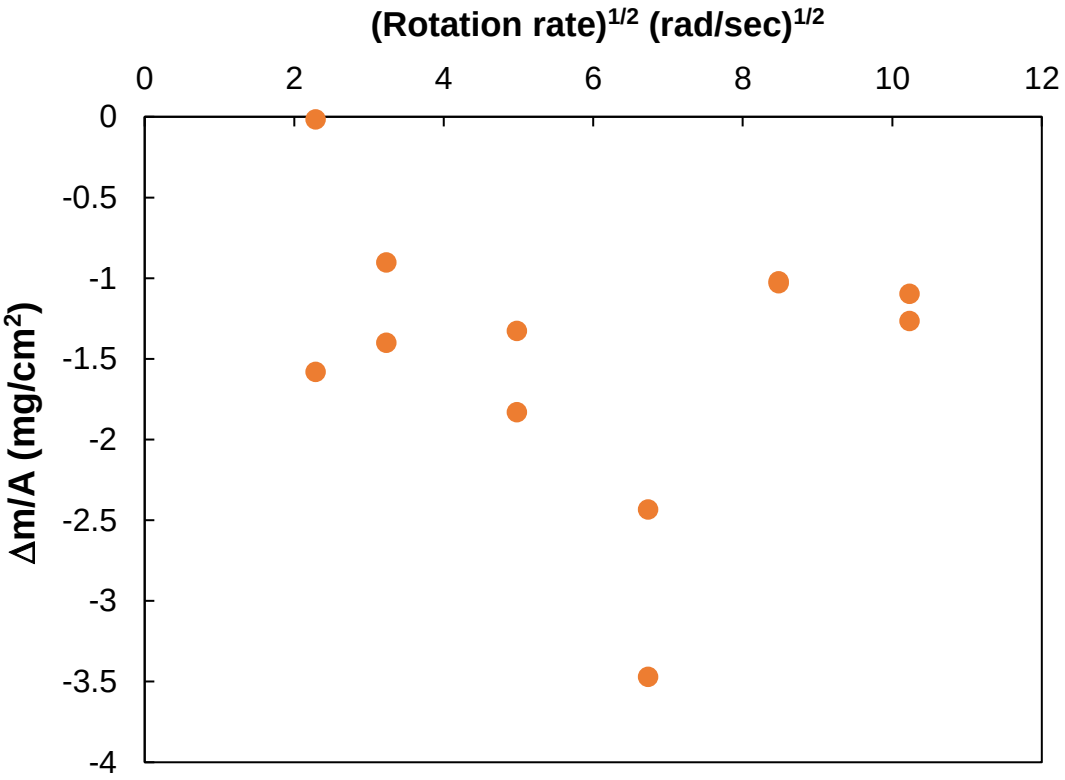

Figure 2.1-3. Plot of the mass change per area, Δm/A, vs. the square root of the specimen rotation rate for H214 specimens exposed to molten $MgCl_2$-KCl-NaCl salt at 750°C for 1 h (after dissolution of adhering, solidified molten salt from the specimens via exposure to water)

change per area, Δm/A, versus the square root of the specimen rotation rate, $\omega^{1/2}$, for molten-salt-exposed H214 specimens is shown in **Figure 2.1-3**. Two separate experiments were conducted at each rotation rate (12 total experiments; the two data points at 433 rpm overlapped). Over the span of rotation rates examined (50-1000 rpm), an increase in the specimen rotation rate (or in the square root of the specimen rotation rate) did not result in an apparent increase in the specimen mass change per area. Appreciable scatter was observed in this data, however, which may have been a result of the incomplete and varied coverage of the specimen surfaces with oxide product (Al_2O_3-MgO-bearing) layers, as discussed below. Given such scatter in the data, and the absence of an apparent trend in the mass change/area with specimen rotation rate, liquid phase diffusion could not be confirmed to be a rate-limiting step for the corrosion of H214 in molten $MgCl_2$-KCl-NaCl at 750°C at low oxygen partial pressures.

After removal of the adherent solidified salt via dissolution in water, scanning electron microscopy was used to characterize the H214 surfaces that had been exposed to the molten $MgCl_2$-KCl-NaCl salt at 750°C. Backscattered electron (BSE) images of such specimen surfaces that had been exposed to the molten salt at rotation rates of 50-1000 rpm are shown in **Figure 2.1-4**. These surfaces contained oxide products (= lower average atomic number dark regions) that partially coated the H214 alloy surface (exposed H214 = higher average atomic number bright regions). Elemental maps

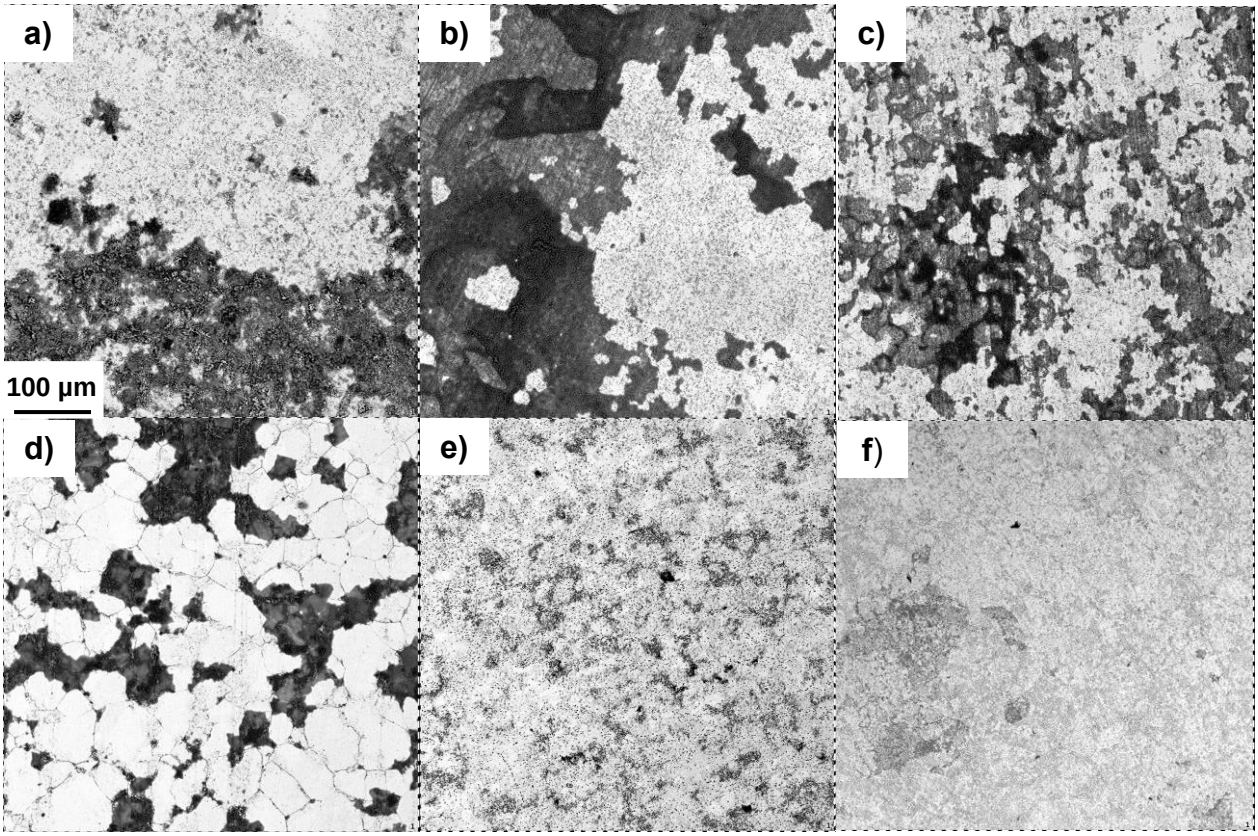

Figure 2.1-4. Top-down backscattered electron (BSE) images of the surfaces of H214 specimens exposed to molten $MgCl_2$-KCl-NaCl salt at 750ºC for 1 h (after dissolution of adhering, solidified molten salt from the specimens via exposure to water) at rotation rates of: **a)** 50 rpm, **b)** 100 rpm, **c)** 237 rpm, **d)** 433 rpm, **e)** 687 rpm, and **f)** 1000 rpm (all images obtained at the same magnification)

obtained by energy dispersive X-ray (EDX) analyses of such specimen surfaces exposed at 100 rpm, 433 rpm, and 1000 rpm to the molten salt are provided in **Figures 2.1-5**, **2.1-6**, and **2.1-7**, respectively. The dark, discontinuous phases seen in the BSE images of these surfaces were found to be Al-O and/or Mg-O rich relative to the brighter, exposed metallic (Ni-Fe-Cr-bearing) phase.

SEM analyses were also conducted on cross-sections of H214 specimens after exposure to the $MgCl_2$-KCl-NaCl salt at 750ºC. BSE images and elemental maps of polished specimen cross-sections of H214 specimens exposed to the $MgCl_2$-KCl-NaCl salt at 750ºC at 100 rpm, 433 rpm, and 1000 rpm are provided in **Figures 2.1-8**, **2.1-9**, and **2.1-10**, respectively. The BSE images revealed thin, relatively bright (relatively high average atomic number) regions (depletion zones) adjacent to the external specimen surfaces that contained reduced concentrations of Cr and Al relative to the bulk alloy.

Thermodynamic analyses were then conducted to evaluate reactions that could have led to surface oxide formation and the depletion zones within the H214 alloy. The oxidation of Cr and Al in the H214 alloy may have occurred by the following reactions:

$$2\{Cr\} + 3/2\ O_2(g) = Cr_2O_3(s) \qquad (4)$$

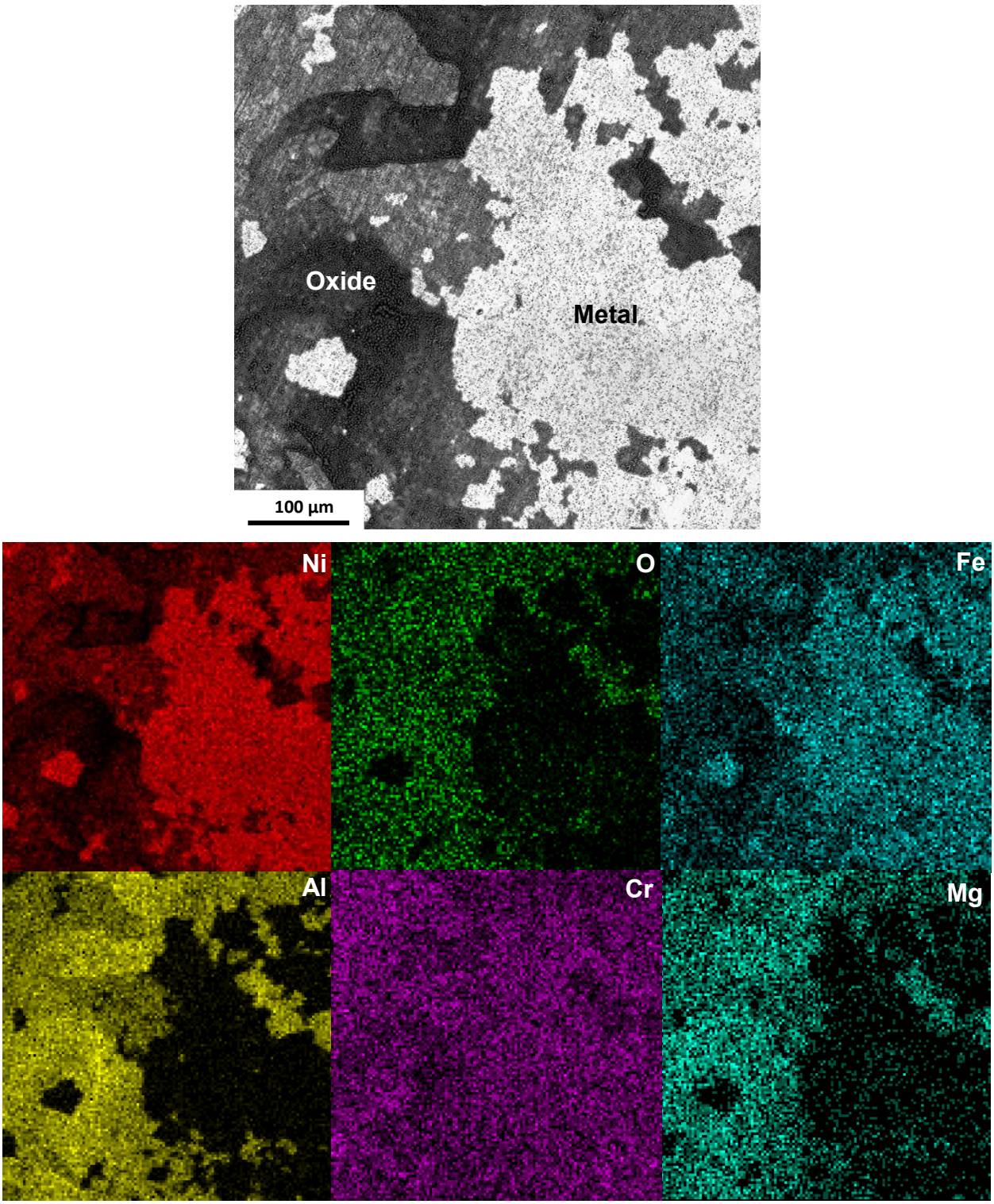

Figure 2.1-5. Top-down backscattered electron (BSE) image (top), and associated elemental maps (below) for Ni, O, Fe, Al, Cr, and Mg, obtained from the surface of a H214 specimen exposed to molten $MgCl_2$-KCl-NaCl salt at 750°C for 1 h at **100 rpm** (after dissolution of adhering, solidified molten salt from the specimens via exposure to water)

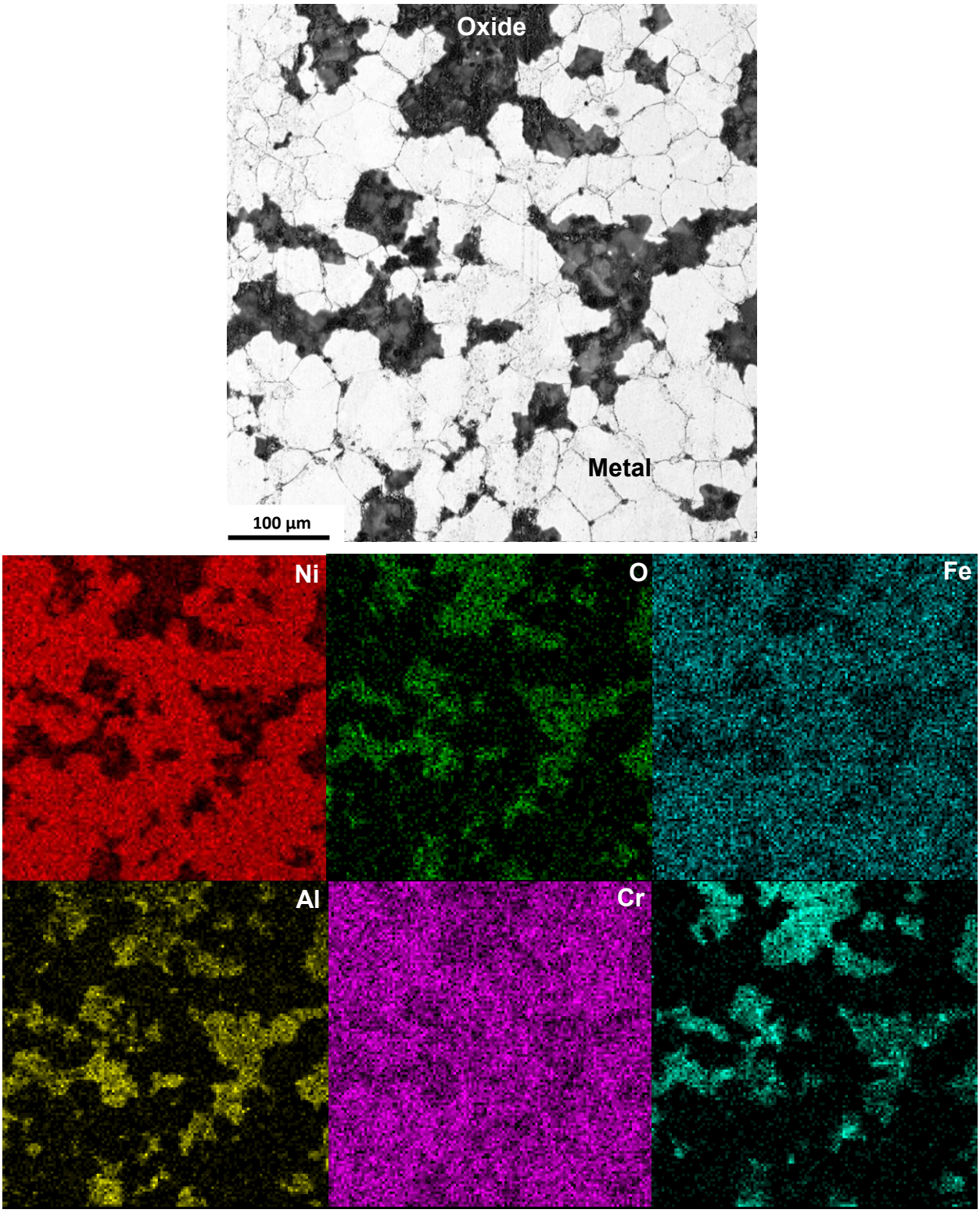

Figure 2.1-6. Top-down backscattered electron (BSE) image (top), and associated elemental maps (below) for Ni, O, Fe, Al, Cr, and Mg, obtained from the surface of a H214 specimen exposed to molten $MgCl_2$-KCl-NaCl salt at 750°C for 1 h at **433 rpm** (after dissolution of adhering, solidified molten salt from the specimens via exposure to water)

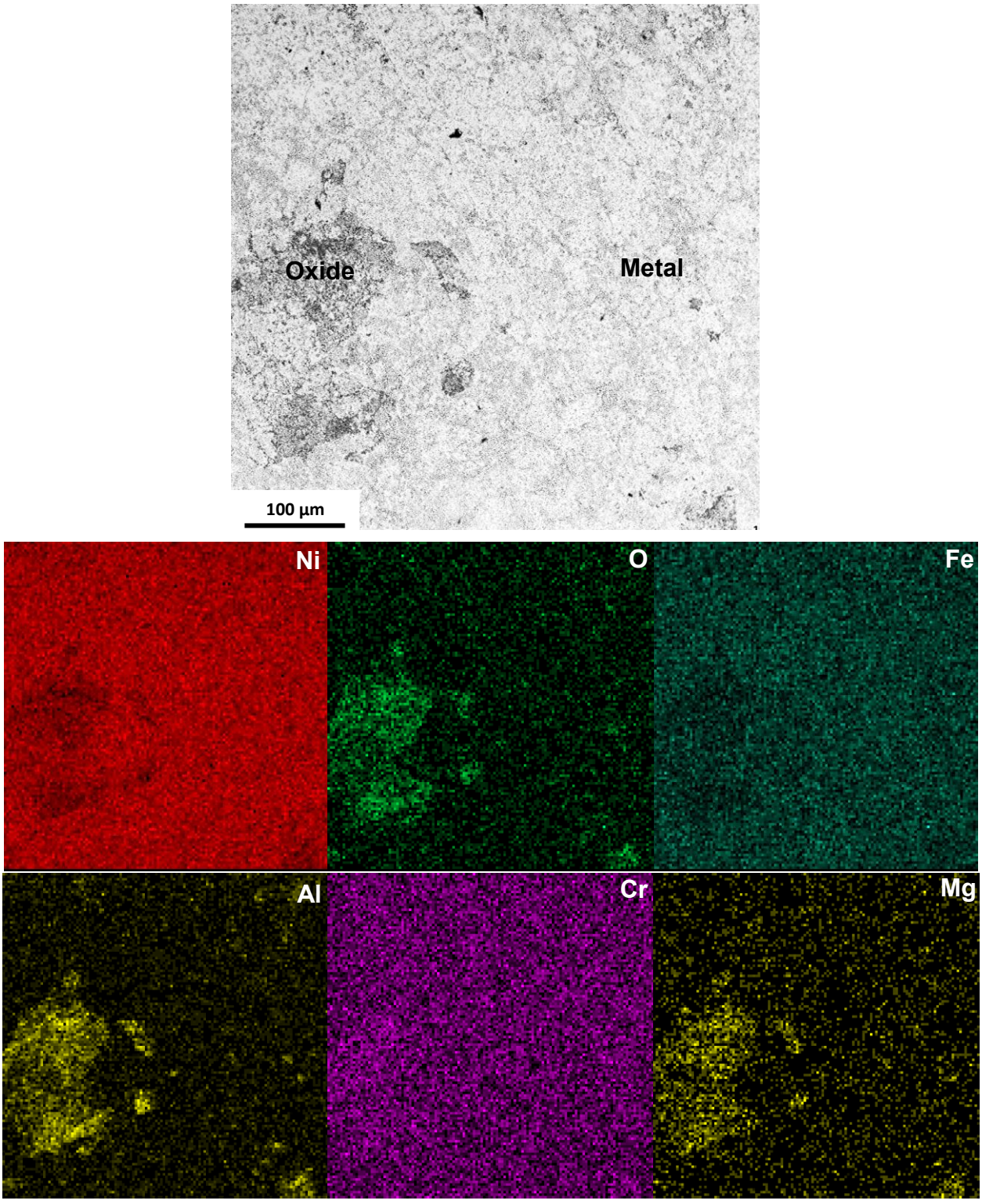

Figure 2.1-7. Top-down backscattered electron (BSE) image (top), and associated elemental maps (below) for Ni, O, Fe, Al, Cr, and Mg, obtained from the surface of a H214 specimen exposed to molten $MgCl_2$-KCl-NaCl salt at 750°C for 1 h at **1000 rpm** (after dissolution of adhering, solidified molten salt from the specimens via exposure to water)

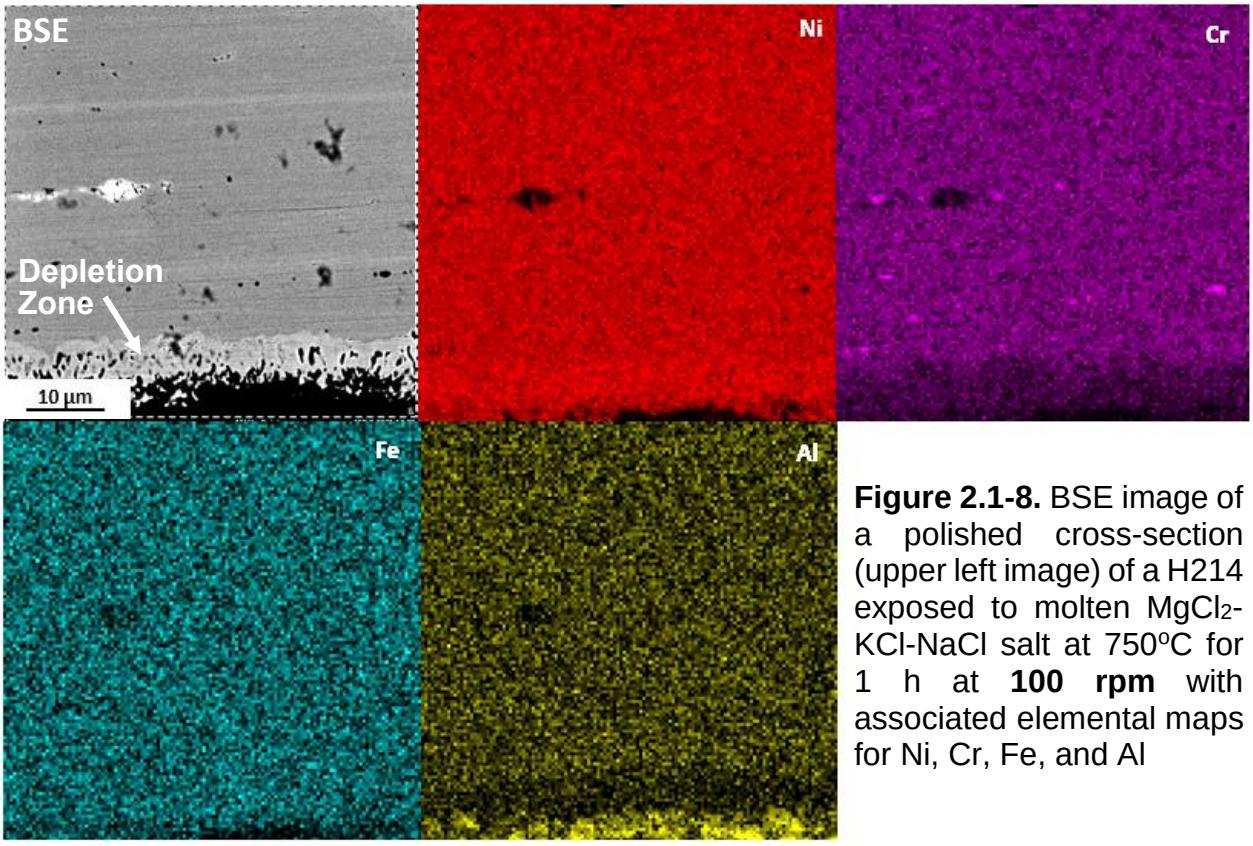

Figure 2.1-8. BSE image of a polished cross-section (upper left image) of a H214 exposed to molten $MgCl_2$-KCl-NaCl salt at 750°C for 1 h at **100 rpm** with associated elemental maps for Ni, Cr, Fe, and Al

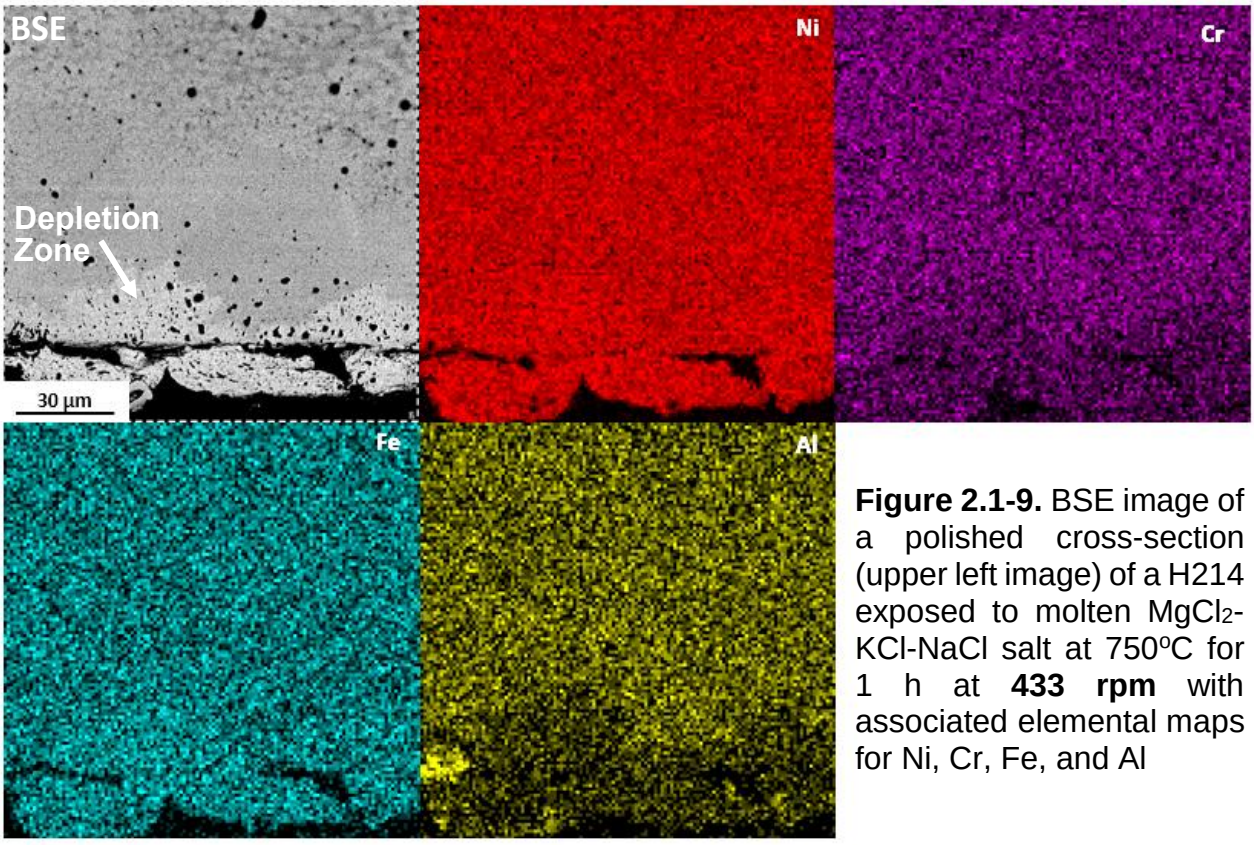

Figure 2.1-9. BSE image of a polished cross-section (upper left image) of a H214 exposed to molten $MgCl_2$-KCl-NaCl salt at 750°C for 1 h at **433 rpm** with associated elemental maps for Ni, Cr, Fe, and Al

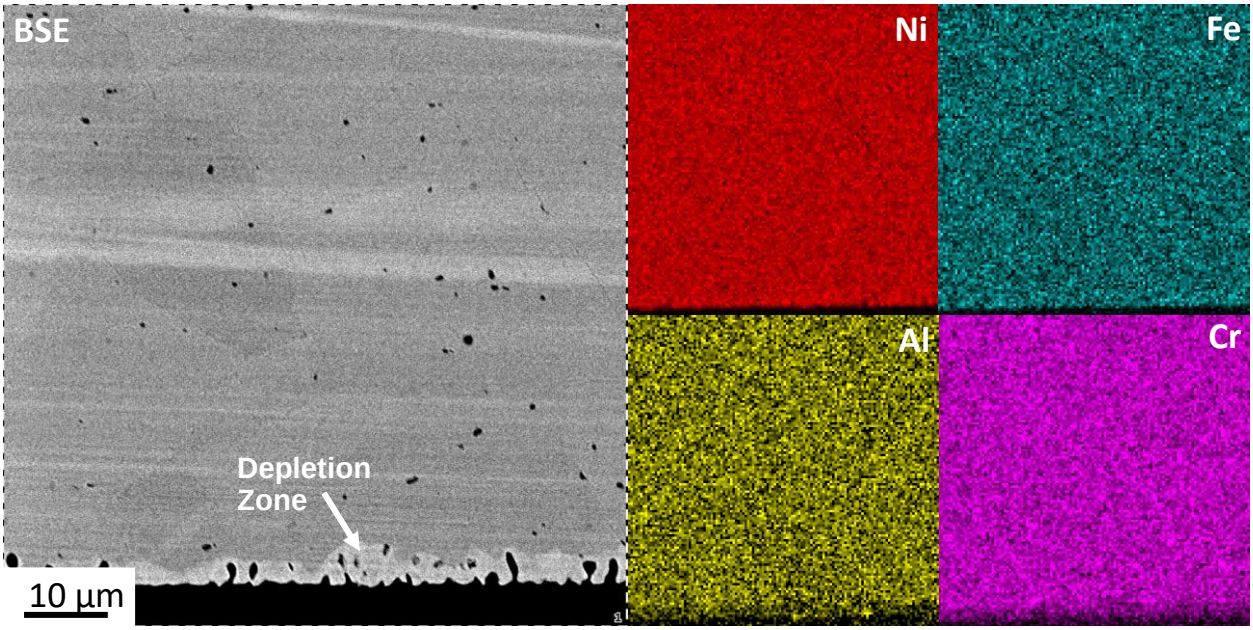

Figure 2.1-10. BSE image of a polished cross-section (left image) of a H214 exposed to molten $MgCl_2$-KCl-NaCl salt at 750°C for 1 h at **1000 rpm** with associated elemental maps for Ni, Fe, Al, and Cr

$$2\{Al\} + 3/2\ O_2(g) = Al_2O_3(s) \quad (5)$$

where {Cr} and {Al} refer to chromium and aluminum dissolved in a Ni-based alloy, respectively. In order for any of these reactions to be thermodynamically favored at 750°C, the alloy must be exposed to a sufficiently high oxygen partial pressure and must possess a sufficiently high activity of a given element at this temperature. The critical oxygen partial pressures (pO_2 values) for the pure elements, and the critical activities of these elements in the alloy at an oxygen partial pressure of 10^{-14} atm (used in this work), required for these oxidation reactions to be thermodynamically favored are shown in **Table 2.1-1**. As can be seen, the critical activities of Cr and Al in the alloy required for oxidation at a pO_2 of 10^{-14} atm at 750°C were both very low; that is, the oxidation of these elements in the alloy was thermodynamically favored.

Table 2.1-1. Thermodynamic calculations for: a) the critical oxygen partial pressures needed to oxidize pure Cr and Al at 750°C and b) the critical activities of Cr and Al dissolved in an alloy at an oxygen partial pressure of 10^{-14} atm at 750°C [16]

Reaction	**Critical pO_2 for oxidation of pure metal at 750°C**	**Critical a_M for oxidation of element M in an alloy at $pO_2 = 10^{-14}$ atm, 750°C**
$2Cr + 3/2\ O_2(g) = Cr_2O_3(s)$	$2.3x10^{-30}$ atm	$1.9x10^{-12}$ ($1.9x10^{-6}$ ppm)
$2Al + 3/2O2(g) = Al_2O_3(s)$	$8.3x10^{-47}$ atm	$8.7x10^{-25}$ ($8.7x10^{-19}$ ppm)

The reaction of these oxides (NiO, FeO, Cr_2O_3, Al_2O_3) with $MgCl_2$ in the molten $MgCl_2$-KCl-NaCl salt to yield MgO via the following displacement reactions may then be considered:

$$3\{MgCl_2\} + Cr_2O_3(s) = 2\{CrCl_3\} + 3MgO(s) \quad (6)$$

$$3\{MgCl_2\} + Al_2O_3(s) = 2\{AlCl_3\} + 3MgO(s) \quad (7)$$

where $\{MgCl_2\}$, $\{CrCl_3\}$, and $\{AlCl_3\}$ refer to magnesium chloride, chromium chloride, and aluminum chloride dissolved in a $MgCl_2$-KCl-NaCl-based melt. Values of the equilibrium reaction constant, K, for these reactions at 750°C or 727°C are shown in **Table 2.1-2** (note: the standard Gibbs free energy of formation of $AlCl_3$ liquid could only be found at up to 727°C). Assuming unit activities for the oxide phases in these reactions (i.e., assuming that the oxides are present in their pure stoichiometric solid oxide reference states), then the activity ratios of the chlorides may be determined, as shown in **Table 2.1-2**. As can be seen from this table, for a given activity of $MgCl_2$ in the $MgCl_2$-KCl-NaCl-based melt, the equilibrium activities of $FeCl_2$ and $CrCl_3$ in such a melt are much higher than for $AlCl_3$. While activity data for $MgCl_2$ in the $MgCl_2$-KCl-NaCl (40-40-20 mol%) liquid at 750°C could not be found for this report, activity data for $MgCl_2$ in $MgCl_2$-KCl liquids at 725°C and 800°C have been published [18,19]. Since the $MgCl_2$:KCl ratio in the $MgCl_2$-KCl-NaCl salts used in the experiments above was 1:1, activity data for an equimolar $MgCl_2$-KCl binary liquid was obtained. The values of $MgCl_2$ activity for a $MgCl_2$-KCl liquid with 50 mol% $MgCl_2$ have been reported to be:

Table 2.1-2. Values for the equilibrium reaction constant, and for the equilibrium chloride activity ratio (assuming that the oxides are present in their pure stoichiometric reference states), for reactions (6) and (7) [16,17]

Reaction	Equilibrium Reaction Constant, K	Equilibrium chloride activity ratio
$3\{MgCl_2\} + Cr_2O_3(s) = 2\{CrCl_3\} + 3MgO(s)$	5.0×10^{-5} (at 750°C)	$(a_{CrCl3})^{2/3}/a_{MgCl2} = 0.037$ (at 750°C)
$3\{MgCl_2\} + Al_2O_3(s) = 2\{AlCl_3\} + 3MgO(s)$	6.4×10^{-12} (at 727°C)	$(a_{AlCl3})^{2/3}/a_{MgCl2} =$ 0.00019 (at 727°C)

$a_{MgCl2}(X_{MgCl2} = 0.50, 725°C) = 0.155$ [reference 18]

$a_{MgCl2}(X_{MgCl2} = 0.50, 800°C) = 0.149$ [reference 19]

Inserting a value of $a_{MgCl2} = 0.15$ into the ratios in **Table 2.1-2** yields the following estimated values for the equilibrium activities of $AlCl_3$ and $CrCl_3$ in the $MgCl_2$-KCl-NaCl liquid:

$$a_{AlCl3} = 1.5\times10^{-7} \text{ (0.15 ppm)}$$

$$a_{CrCl3} = 4.1\times10^{-4} \text{ (410 ppm)}$$

These calculations indicated that Al_2O_3 should stop dissolving (via reaction (7)) in the

$MgCl_2$-KCl-NaCl liquid at 750°C after minimal initial dissolution (until the $AlCl_3$ activity in the melt reaches 0.15 ppm), whereas Cr_2O_3 can exhibit more dissolution (via reaction (6)) upon equilibration and contribute more appreciably to the formation of MgO under equilibrium conditions. This thermodynamic analyses was consistent with the retention of Al_2O_3 particles at the specimen surfaces (**Figures 2.1-5**, **2.1-6**, and **2.1-7**), and the depletion of Cr from the alloy (**Figures 2.1-8**, **2.1-9**, and **2.1-10**).

BSE images of polished cross-sections of molten-salt-exposed H214 specimens, of the type shown in **Figures 2.1-8**, **2.1-9**, and **2.1-10**, were used to evaluate the average thicknesses of the depletion zones generated within these specimens. A plot of the average depletion zone thickness versus the H214 specimen rotation rate, ω, is shown in **Figure 2.1-11**. A plot of the average depletion zone thickness versus the square root of the specimen rotation rate, $\omega^{1/2}$, is shown in **Figure 2.1-12**. Over the range of rotation rates examined (50 rpm to 1000 rpm), an increase in the specimen rotation rate (or in the square root of the specimen rotation rate) did not result in an apparent increase in the depletion zone thickness. However, appreciable scatter was also observed in this kinetic data. Hence, as discussed above for the mass change measurements, the depletion zone thickness measurements could not be used to confirm that liquid phase diffusion was a rate-limiting step for the corrosion of H214 in molten $MgCl_2$-KCl-NaCl at 750°C and at low oxygen partial pressures.

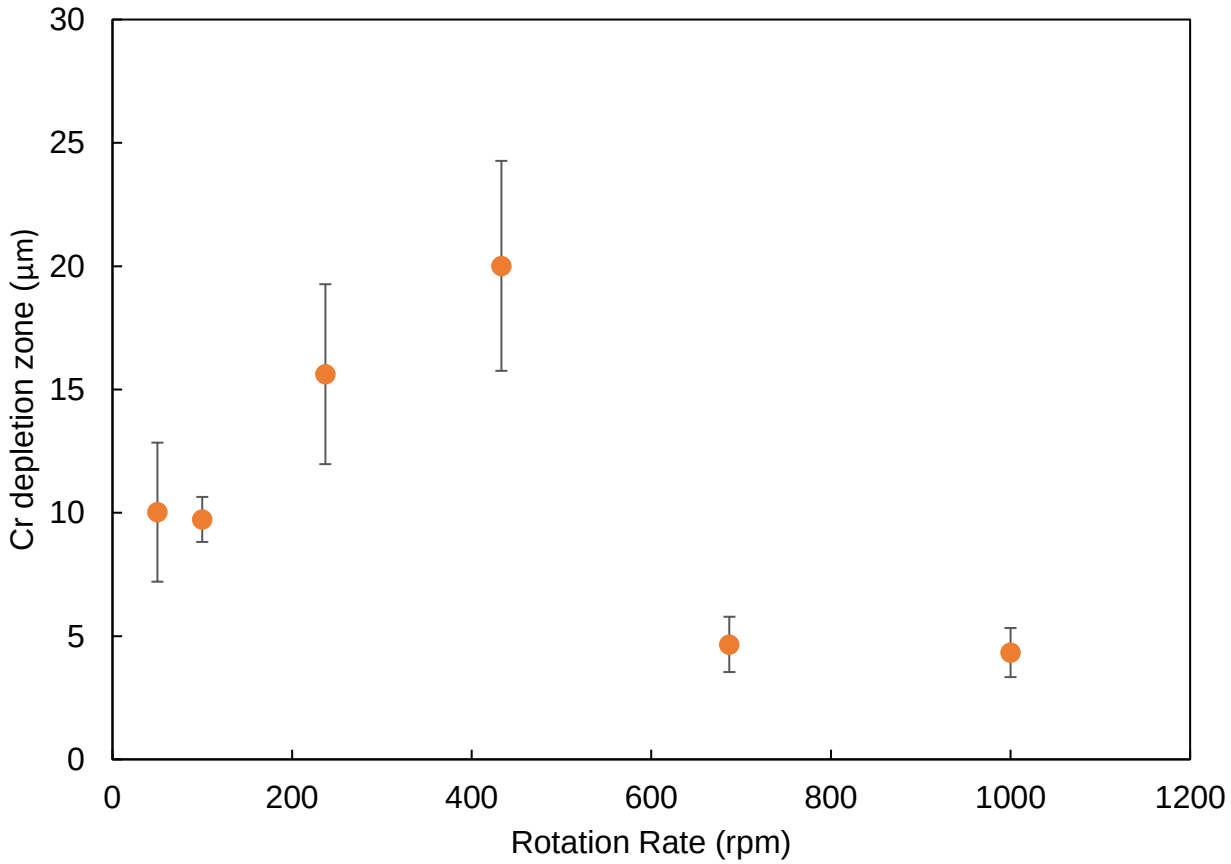

Figure 2.1-11. Plot of the depletion zone thickness vs. the specimen rotation rate for H214 specimens exposed to molten $MgCl_2$-KCl-NaCl salt at 750°C for 1 h

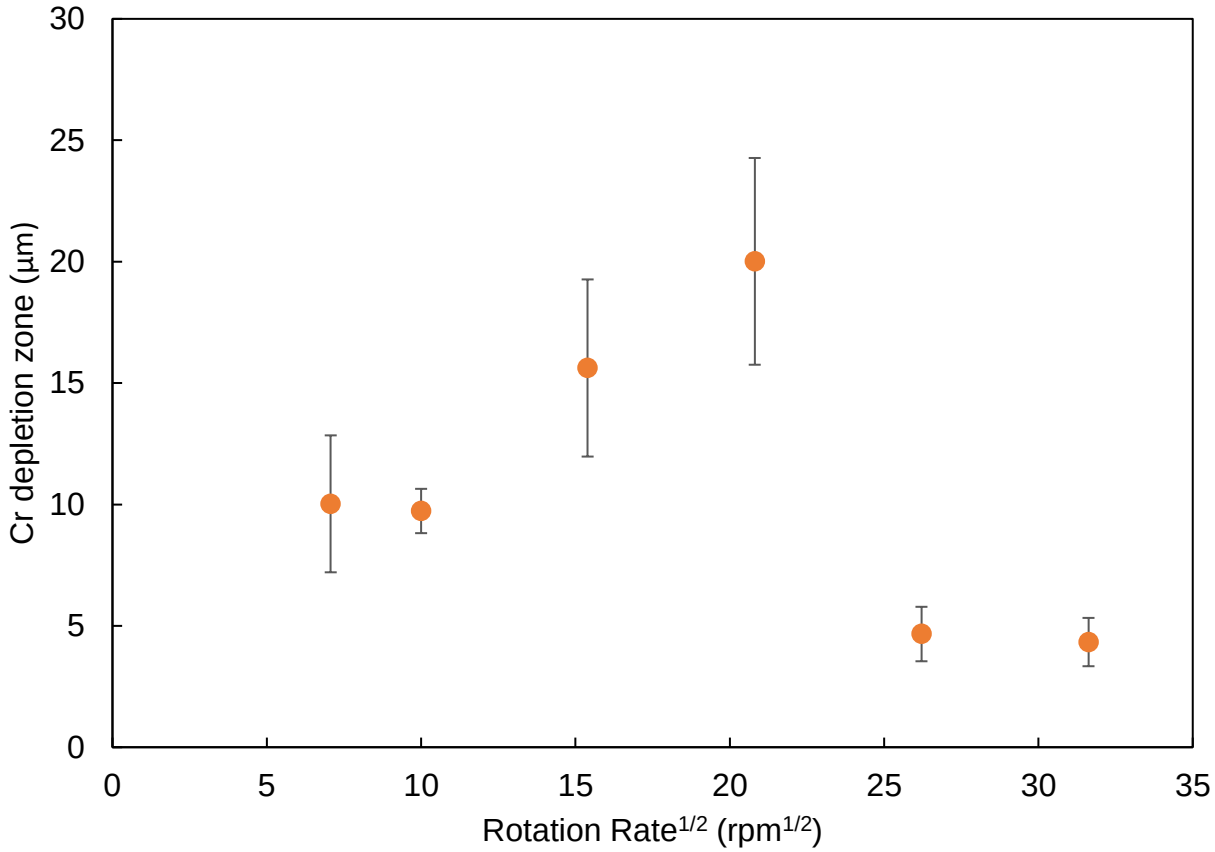

Figure 2.1-12. Plot of the depletion zone thickness vs. the square root of the specimen rotation rate for H214 specimens exposed to molten $MgCl_2$-KCl-NaCl at 750°C for 1 h

Subtask 2.2: Corrosion at High Oxygen Partial Pressures

Due to the delays caused by the 3-month COVID19 lab shutdown, and the associated budget restrictions imposed by this shutdown, work on this task was stopped. After the lab reopened, the effort in Task 2.0 was focused on completing Subtask 2.1 (evaluating corrosion in molten $MgCl_2$-KCl-NaCl salts under forced-convective conditions at low oxygen partial pressures).

Task 3.0: Minimize Corrosion Kinetics

Milestone 3: Determine the atmospheric, chemical, and fluid dynamic conditions required to achieve projected annual corrosion of <30 µm/year for metal alloys and ceramic composites in molten chloride salts at CSP-relevant temperatures

Subtask 3.1: Tailoring Corrosion Conditions at Low Oxygen Partial Pressures

Due to the delays caused by the 3-month COVID19 lab shutdown, and the associated budget restrictions imposed by this shutdown, work on this task was stopped. After the lab reopened, the effort in Task 3 was focused on identifying molten salt and specimen surface conditions that would minimize corrosion at high oxygen partial pressures for Subtask 3.2 (in parallel with the rotating-disk corrosion experiments for Subtask 2.1).

Subtask 3.2: Tailoring Corrosion Conditions at High Oxygen Partial Pressures

While use of the rotating-disk corrosion test apparatus was committed towards experiments with H214 specimens in molten $MgCl_2$-KCl-NaCl (40-40-20 mole%) salt, parallel work was conducted to:

- identify and demonstrate alternate earth-abundant molten chlorides that are more resistant to oxidation in air than molten $MgCl_2$-KCl-NaCl salts, and
- identify and demonstrate a strategy for containment of such air-stable molten chlorides

Thermodynamic Analyses

The following reactions may be considered to evaluate the relative resistances of $MgCl_2$, $CaCl_2$, $SrCl_2$, $BaCl_2$, NaCl, and KCl to reaction with oxygen-bearing and water-vapor-bearing atmospheres at 750°C:

$MgCl_2 + ½O_2(g) \leftrightarrow MgO + Cl_2(g)$ (8a)
$\Delta G°_{rxn}$(8a) [750°C] = -44.3 kJ/mole

$MgCl_2 + H_2O(g) \leftrightarrow MgO + 2HCl(g)$ (8b)
$\Delta G°_{rxn}$(8b) [750°C] = -54.7 kJ/mole

$CaCl_2 + ½O_2(g) \leftrightarrow CaO + Cl_2(g)$ (9a)
$\Delta G°_{rxn}$(9a) [750°C] = +143.1 kJ/mole

$CaCl_2 + H_2O(g) \leftrightarrow CaO + 2HCl(g)$ (9b)
$\Delta G°_{rxn}$(9b) [750°C] = +132.7 kJ/mole

$SrCl_2 + ½O_2(g) \leftrightarrow SrO + Cl_2(g)$ (10a)
$\Delta G°_{rxn}$(10a) [750°C] = +180.3 kJ/mole

$SrCl_2 + H_2O(g) \leftrightarrow SrO + 2HCl(g)$ (10b)
$\Delta G°_{rxn}$(10b) [750°C] = +169.8 kJ/mole

$BaCl_2 + ½O_2(g) \leftrightarrow BaO + Cl_2(g)$ (11a)
$\Delta G°_{rxn}$(11a) [750°C] = +240.2 kJ/mole

$BaCl_2 + H_2O(g) \leftrightarrow BaO + 2HCl(g)$ (11b)
$\Delta G°_{rxn}$(11b) [750°C] = +229.8 kJ/mole

$2NaCl + ½O_2(g) \leftrightarrow Na_2O + Cl_2(g)$ (12a)
$\Delta G°_{rxn}$(12a) [750°C] = +356.0 kJ/mole

$2NaCl + H_2O(g) \leftrightarrow Na_2O + 2HCl(g)$ (12b)
$\Delta G°_{rxn}$(12b) [750°C] = +345.6 kJ/mole

$2KCl + ½O_2(g) \leftrightarrow K_2O + Cl_2(g)$ (13a)
$\Delta G°_{rxn}$(13a) [750°C] = +457.6 kJ/mole

$2KCl + H_2O(g) \leftrightarrow K_2O + 2HCl(g)$ (13b)
$\Delta G°_{rxn}$(13b) [750°C] = +447.2 kJ/mole

The values of the standard Gibbs free energy change for these reactions [16,17] at 750°C,

$\Delta G°_{rxn}$ [750°C], are also shown above. These $\Delta G°_{rxn}$ values indicate that the oxidation of $CaCl_2$, $SrCl_2$, $BaCl_2$, NaCl, and KCl can be much less favored than for $MgCl_2$ oxidation.

Consider, as comparative examples, the oxidation of $MgCl_2$ dissolved in a eutectic $MgCl_2$-KCl melt (32±2 mol% $MgCl_2$; T_{eut} = 433±9°C [6,16,17,20-23]) and the oxidation of $CaCl_2$ dissolved in a eutectic $CaCl_2$-NaCl melt (52+2 mol% $CaCl_2$; T_{eut} = 500±8°C [24-28]). Using activity data [19] reported for $MgCl_2$ in a $MgCl_2$(32 mol%)-KCl melt, and assuming a unit activity for MgO(s) and that chlorine, oxygen, and water vapor behave as ideal gases, the equilibrium partial pressure ratios, $p[Cl_2]/(p[O_2])^{1/2}$ and $(p[HCl])^2/p[H_2O]$, for the oxidation of $MgCl_2$ in this melt by reactions (8a) and (8b) at 750°C were found to be 3.0 and 10.2, respectively. Consequently, the oxidation of $MgCl_2$ in this $MgCl_2$-KCl liquid via reaction with oxygen in dry air (oxygen partial pressure, $p[O_2]$ = 0.21 atm), or via reaction with water vapor at a partial pressure of $2.3x10^{-3}$ atm (corresponding to the $p[H_2O]$ of the ambient lab air in this work), will be favored unless the effective equilibrium chlorine partial pressure, $p[Cl_2]$, or effective hydrochloric acid vapor partial pressure, p[HCl], exceed 1.4 atm or 0.15 atm, respectively.

Using activity data for $CaCl_2$ in a $CaCl_2$(53 mol%)-NaCl melt [19], with a unit activity for CaO(s) and assuming ideal gas behavior for chlorine, oxygen, and water vapor, equilibrium partial pressure ratios, $p[Cl_2]/(p[O_2])^{1/2}$ and $(p[HCl])^2/p[H_2O]$, for the oxidation of $CaCl_2$ in this melt by reactions (9a) and (9b) at 750°C in this melt at 750°C were found to be $2.3x10^{-8}$ and $8.0x10^{-8}$, respectively. Consequently, the oxidation of $CaCl_2$ in this $CaCl_2$-NaCl liquid via reaction with oxygen in dry synthetic air, or via reaction with water vapor at a partial pressure of $2.3x10^{-3}$ atm, will not be thermodynamically favored once the local effective chlorine partial pressure or water vapor partial pressure exceeds $1.1x10^{-8}$ atm (11 ppb) or $1.4x10^{-5}$ atm (14 ppm), respectively.

Similar calculations using thermodynamic data [16,19] for eutectic $SrCl_2$-NaCl (52 mol% $SrCl_2$, 48 mol% NaCl; T_{eut} = 565°C [29]) and $BaCl_2$-NaCl liquids (40 mol% $BaCl_2$, 60 mol% NaCl; T_{eut} = 651°C [30]) yield even smaller values for the equilibrium chlorine partial pressures or water vapor partial pressures required to avoid $SrCl_2$ and $BaCl_2$ oxidation in such liquids in dry air, or in water vapor at a partial pressure of $2.3x10^{-3}$ atm, respectively, at 750°C. Hence, the oxidation of $CaCl_2$, $SrCl_2$, and $BaCl_2$ present in eutectic $CaCl_2$-NaCl, $SrCl_2$-NaCl, and $BaCl_2$-NaCl liquids, respectively, by reaction with oxygen in dry air, or with water vapor at a partial pressure of $2.3x10^{-3}$ atm, at 750°C are much less strongly favored than the oxidation of $MgCl_2$ dissolved in the eutectic $MgCl_2$-KCl liquid under similar conditions.

In order to utilize such air-stable molten chlorides for high-temperature heat transfer and thermal energy storage for CSP plants, corrosion-resistant pipes and tanks are required for the containment of such molten salts. Consider the following reactions of NiO, Cr_2O_3, and Al_2O_3 with chlorine and hydrochloric acid vapor:

$$NiO + Cl_2(g) \leftrightarrow NiCl_2 + ½O_2(g) \quad (14a)$$

$$\Delta G°_{rxn}(14a)\ [750°C] = -5.7\ kJ/mole$$

$$NiO + 2HCl(g) \leftrightarrow NiCl_2 + H_2O(g) \quad (14b)$$

$$\Delta G°_{rxn}(14b)\ [750°C] = +4.7\ kJ/mole$$

$$1/3Cr_2O_3 + Cl_2(g) \leftrightarrow 2/3CrCl_3 + ½O2(g) \quad (15a)$$

$$\Delta G°_{rxn}(15a)\ [750°C] = +72.3\ kJ/mole$$

$1/3Cr_2O_3 + 2HCl(g) \leftrightarrow 2/3CrCl_3 + H_2O(g)$ (15b)

$\Delta G°_{rxn}$(15b) [750°C] = +82.8 kJ/mole

$1/3Al_2O_3 + Cl_2(g) \leftrightarrow 2/3AlCl_3 + ½O_2(g)$ (16a)

$\Delta G°_{rxn}$(16a) [750°C] = +115.5 kJ/mole

$1/3Al_2O_3 + 2HCl(g) \leftrightarrow 2/3AlCl_3 + H_2O(g)$ (16b)

$\Delta G°_{rxn}$(16b) [750°C] = 125.9 kJ/mole

The calculated equilibrium partial pressure ratios, $p[Cl_2]/(p[O_2])^{1/2}$ and $(p[HCl])^2/p[H_2O]$, associated with the oxidation of $CaCl_2$ in a molten $CaCl_2$(53 mol%)-NaCl salt by reactions (9a) and (9b) at 750°C were found to be $2.3x10^{-8}$ and $8.0x10^{-8}$, respectively. For these $p[Cl_2]/(p[O_2])^{1/2}$ and $(p[HCl])^2/p[H_2O]$ values, pure solid NiO, Cr_2O_3, and Al_2O_3 can undergo reaction with this $CaCl_2$-NaCl liquid only if the activities of the chloride products dissolved in the melt are sufficiently low. The critical activities of $NiCl_2$, $CrCl_3$, and $AlCl_3$ associated with the equilibrium of reaction (9a) with reactions (14a), (15a), or (16a), respectively, for molten $CaCl_2$(53 mol%)-NaCl salt at 750°C were found to be $4.6x10^{-8}$, $1.0x10^{-17}$, or $5.1x10^{-21}$, respectively [16,17]. The same extremely low critical activity values of $NiCl_2$, $CrCl_3$, and $AlCl_3$ were associated with the equilibrium of reaction (9b) with reactions (14b), (15b), or (16b), respectively, with this $CaCl_2$-NaCl salt at 750°C. Hence, after very small amounts of chloride product formation and dissolution, these oxides should become thermodynamically stable with the eutectic $CaCl_2$-NaCl melt in dry air, or in water vapor at a partial pressure of $2.3x10^{-3}$ atm, at 750°C. Consequently, external NiO, Cr_2O_3, or Al_2O_3 scales formed upon oxidation of solid metal or alloy pipes and tanks, or such oxides present in ceramic-lined pipes and tanks, should become resistant to reaction with $CaCl_2$-NaCl melts saturated with dry air, or saturated with such a water vapor-bearing atmosphere, after minimal interaction with such liquids.

Demonstration of $CaCl_2$-NaCl Oxidation Resistance in Ambient Air

In light of the thermodynamic analyses above, the relative resistances of $MgCl_2$, dissolved in a $MgCl_2$(32 mol%)-KCl liquid, and of $CaCl_2$, dissolved in a $CaCl_2$(53 mol%)-NaCl liquid, towards high-temperature oxidation have been examined by exposing these molten salts to ambient lab air (with a water vapor partial pressure of $2.3x10^{-3}$ atm), and to dry Ar, at 750°C. Room-temperature X-ray diffraction (XRD) patterns obtained from these salts before and after such exposures are provided in **Figure 3.2-1**. After only 2.5 h of exposure of the $MgCl_2$-KCl salt to ambient air at 750°C, the presence of appreciable MgO was detected within this solidified salt (**Figure 3.2-1b**) along with residual KCl and K_2MgCl_4 (this latter compound was the predominant phase detected in the solidified $MgCl_2$-KCl salt prepared prior to such high-temperature ambient air exposure, **Figure 3.2-1a**) [31]. On the other hand, only diffraction peaks for $CaCl_2$ and NaCl (i.e., not for CaO) were detected in the solidified $CaCl_2$-NaCl salt before and after exposure for 50 h to ambient air at 750°C (Figures **3.2-1c and d**) [31].

Weight change measurements were also used to evaluate the relative oxidation resistances of the molten $MgCl_2$-KCl and $CaCl_2$-NaCl salts. Complete oxidation of the $MgCl_2$ in a $MgCl_2$(32 mol%)-KCl liquid via reaction (8a) or (8b) should result in a 21.7% weight loss, whereas complete oxidation of the $CaCl_2$ in a $CaCl_2$(53 mol%)-NaCl liquid via reaction (9a) or (9b) should result in a 33.7% weight loss. Exposure of the molten

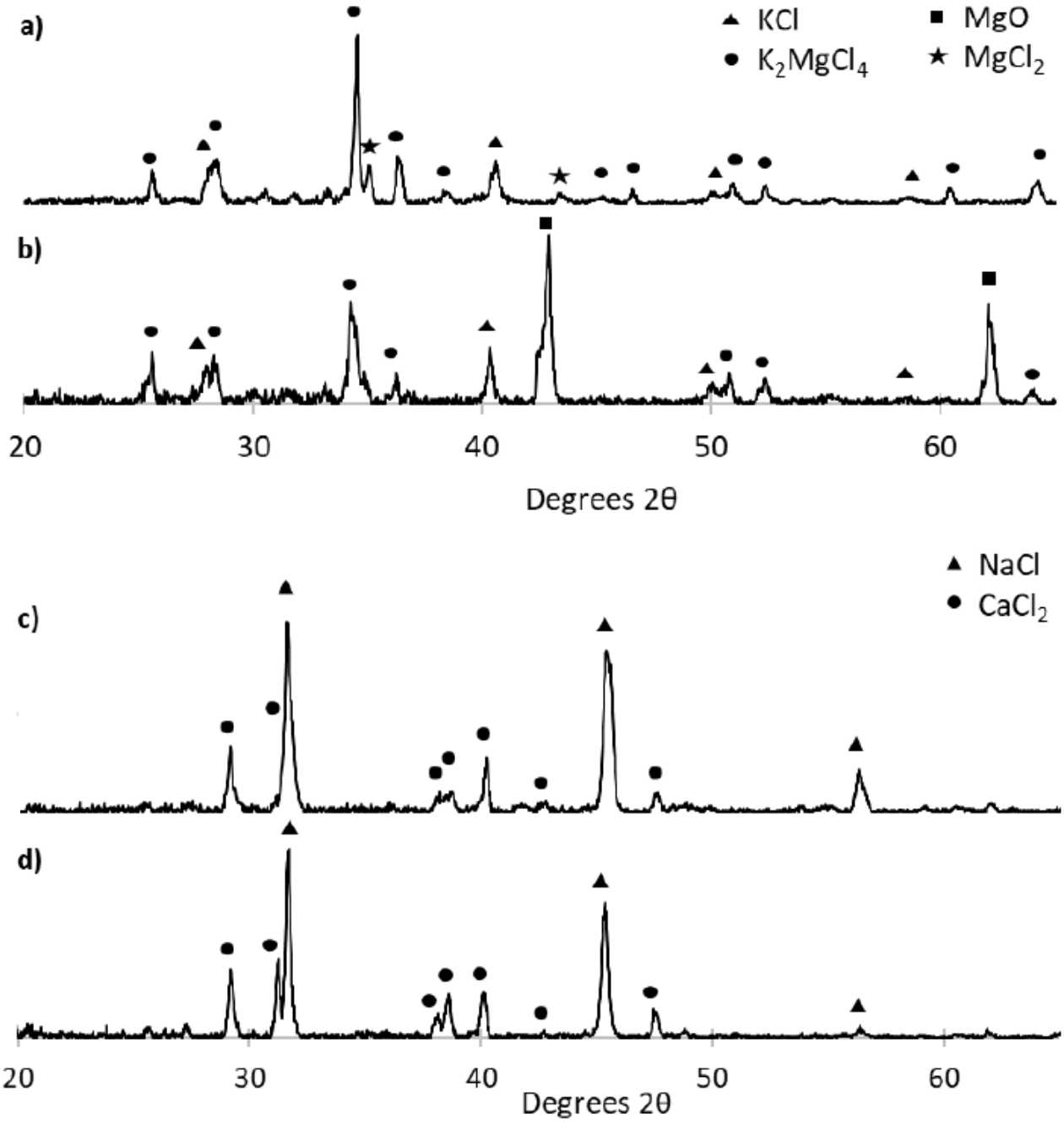

Figure 3.2-1. Relative stabilities of molten $MgCl_2$-KCl and $CaCl_2$-NaCl salts in air and Ar at 750°C. Room temperature X-ray diffraction patterns obtained from: **a)** a $MgCl_2$(32 mol%)-KCl salt after exposure to dry, high-purity Ar for 50 h at 750°C, **b)** the $MgCl_2$(32 mol%)-KCl salt after exposure to ambient air (water vapor partial pressure of $2.3x10^{-3}$ atm) for 2.5 h at 750°C, **c)** a $CaCl_2$(53 mol%)-NaCl salt after exposure to dry, high-purity Ar for 50 h at 750°C, **d)** the $CaCl_2$(53 mol%)-NaCl salt after exposure to ambient air (water vapor partial pressure of $2.3x10^{-3}$ atm) for 50 h at 750°C

$MgCl_2$-KCl salt to stagnant ambient air for 2.5 h at 750°C resulted in a weight loss of 15.3±1.1%, which was consistent with appreciable $MgCl_2$ oxidation (as also indicated by the detection of appreciable MgO in the XRD pattern in **Figure 3.2-1b**). Exposure of the molten $CaCl_2$-NaCl salt to stagnant ambient air for 2.5 h at 750°C resulted in a significantly smaller weight loss of 0.3±0.2%. This latter small weight loss was similar to the weight loss detected upon exposure of the molten $CaCl_2$-NaCl salt to stagnant dry Ar for 2.5 h at 750°C (0.2±0.1%), which indicated that such small weight losses were due to a modest amount of salt evaporation.

The extensive oxidation of $MgCl_2$ present in the $MgCl_2$-KCl melt in ambient air at 750°C (from XRD and weight change analyses), and the lack of detectable oxidation of the molten $CaCl_2$-NaCl salt under similar conditions, were consistent with the thermodynamic calculations above; that is, the molten $CaCl_2$-NaCl salt was significantly more resistant to oxidation in ambient air at 750°C than was the molten $MgCl_2$-KCl salt.

Demonstration of Corrosion-Resistant Containment of Molten $CaCl_2$-NaCl in Air

To demonstrate the corrosion-resistant containment of the air-stable molten $CaCl_2$-NaCl salt, pre-oxidized, plate-shaped Ni specimens (with continuous external NiO scales) were exposed (in a vertical orientation) to molten $CaCl_2$-NaCl salts in ambient air at 750°C for up to 48 h. Two types of molten salts were utilized in these corrosion experiments, in order to examine the influence of the starting nickel content of the salt on such corrosion: $CaCl_2$(53 mol%)-NaCl salts that had been presaturated with NiO at 750°C in air, and $CaCl_2$(53 mol%)-NaCl without such NiO presaturation. Inductively-coupled plasma-mass spectroscopic analyses indicated that the NiO-saturated molten $CaCl_2$-NaCl salt contained a nickel content of 27.5±9.7 ppm (atomic basis).

Plots of the NiO/Ni specimen mass change per area, Δm/A, as a function of immersion time in these molten salts are shown in **Figures 3.2-2a** and **b**. The pre-oxidized Ni specimens exhibited a modest mass gain with immersion time in the molten $CaCl_2$-NaCl salt at 750°C in ambient air. Similar Δm/A values were obtained for corrosion of these specimens in molten $CaCl_2$-NaCl salts with or without presaturation with NiO. As shown in **Figure 3.2-2b**, a good fit was obtained to parabolic kinetics (Δm/A vs. $t^{1/2}$), with the best fit line yielding yielded a slope of 5.9±0.4 x10^{-7} g/cm^{2}s$^{1/2}$ (3.5±0.2x10^{-2} mg/cm^{2}h$^{1/2}$). This value was not far from the measured rate of mass change per area for NiO-bearing (pre-oxidized) Ni specimens exposed only to air at 750°C. Thermogravimetric analysis of pre-oxidized Ni in flowing synthetic dry air at 750°C yielded a parabolic plot with a fitted slope of 8.2±0.9x10^{-7} g/cm^{2}s$^{1/2}$ (4.9±0.5x10^{-2} mg/cm^{2}h$^{1/2}$). The following expression has also been reported for the rate of oxidation of Ni specimens (at >1100°C) that had first been pre-oxidized at 1400°C [32] (i.e., a similar pre-oxidation temperature as used in the present work):

$$k_p = 0.377(p[O_2])^{1/12}\exp[-119.5\ \text{kJ mol}^{-1}\ R^{-1}\ T^{-1}]\ \text{g/cm}^2\text{s}^{1/2}$$

The extrapolated k_p value obtained from this equation for air at 750°C (i.e., $p[O_2]$ = 0.21 atm, 1023 K) was 2.6x10^{-7} g/cm^{2}s$^{1/2}$. This extrapolated value was also not far (within a factor of 2.3) from the corrosion rate obtained in molten $CaCl_2$-NaCl salt in the present work. The similarity in the observed rates for the oxidation of NiO/Ni specimens in air at 750°C and for the corrosion of NiO/Ni specimens in the molten $CaCl_2$-NaCl salt in air at750°C was consistent with a similar rate-controlling mechanism for the oxidation of NiO-bearing Ni specimens in both environments, namely, solid-state diffusion through the NiO

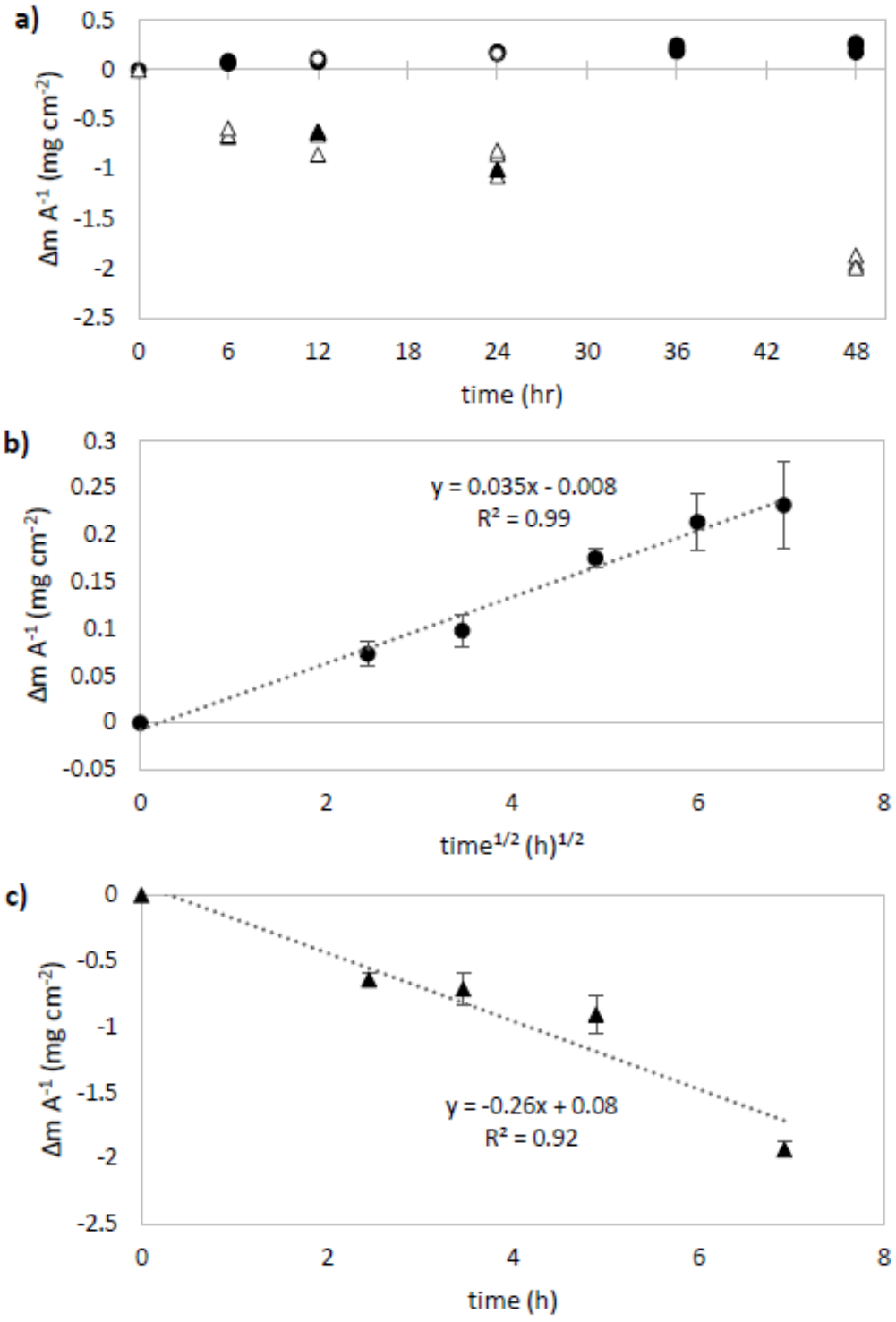

Figure 3.2-2. Corrosion kinetics of NiO/Ni (pre-oxidized Ni) and Ni specimens in molten $CaCl_2$(53 mol%)-NaCl salt in air at 750°C: **a)** Δm/A vs. time plot for exposure of NiO/Ni (circles) and as-polished Ni (triangle) specimens to the molten $CaCl_2$-NaCl salt that had (closed symbols) or had not (open symbols) been pre-saturated with NiO, **b)** Parabolic (Δm/A vs. $(time)^{1/2}$) plot for NiO/Ni exposure to molten $CaCl_2$-NaCl, **c)** Linear (Δm/A vs. time) plot for exposure of as-polished Ni specimens to the molten $CaCl_2$-NaCl salt

scale (via outward Ni cation migration) [32].

A backscattered electron (BSE) image, and associated elemental maps (from energy-dispersive X-ray (EDX) analyses), of a polished cross-section of the interface between a pre-oxidized Ni specimen and solidified $CaCl_2$-NaCl salt, after exposure of the specimen to the molten salt for 48 h in air at 750°C, are shown in **Figure 3.2-3**. The elemental maps indicated that the molten $CaCl_2$-NaCl salt did not penetrate through the NiO scale, so that continued oxidation of the underlying Ni exposed to this molten salt in air at 750°C required solid-state diffusion through the NiO scale. The parabolic corrosion rate obtained for the pre-oxidized Ni specimens in the molten $CaCl_2$-NaCl salt in air at 750°C corresponded to an annual mass change per area value of 3.4×10^{-3} g/cm^2, or an annual Ni recession (with the molar volume of Ni = 6.59 cm^3/mole [31]) of only 14 μm, ***consistent with Milestone 3***.

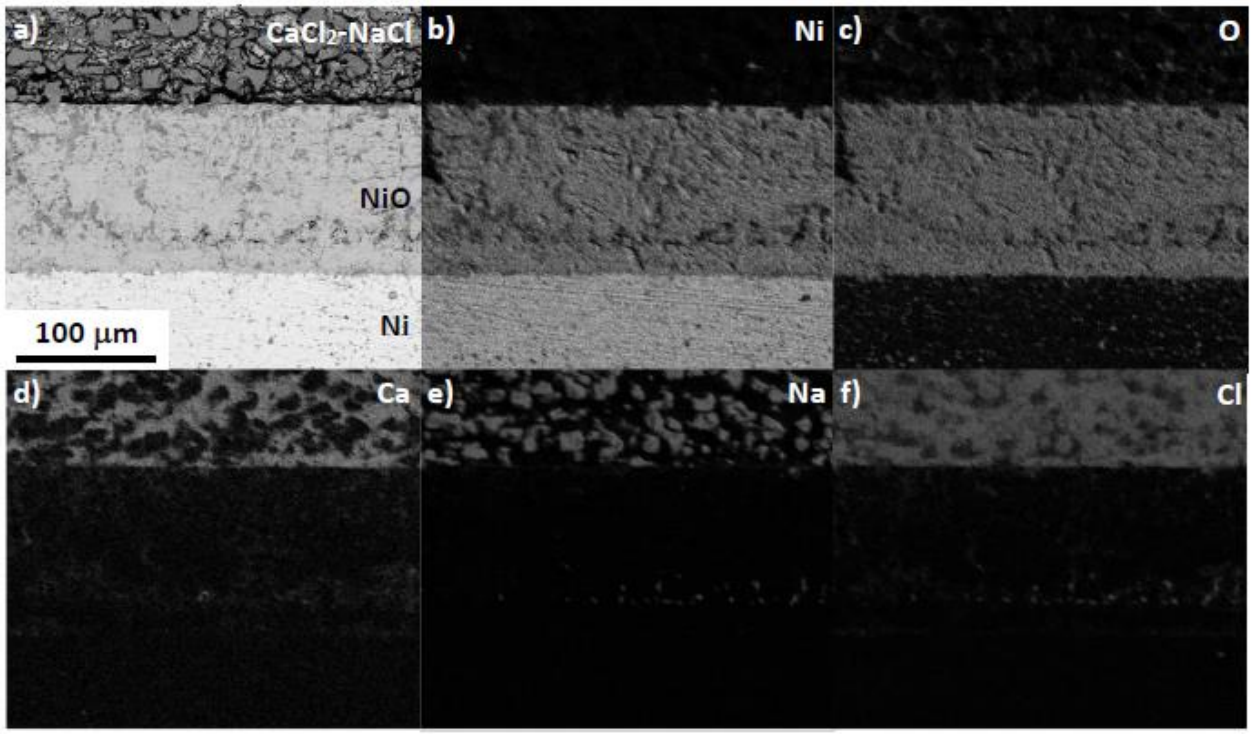

Figure 3.2-3. The interface between a pre-oxidized Ni specimen and solidified $CaCl_2$-NaCl liquid: **a)** BSE image and **b)-f)** associated elemental maps for Ni, O, Ca, Na, and Cl, respectively, obtained from a polished cross-section of a pre-oxidized Ni (NiO/Ni) sample that had been exposed to a $CaCl_2$(53 mol%)-NaCl liquid for 48 h in ambient air at 750°C

Experiments were also conducted to evaluate the corrosion of as-polished Ni specimens (i.e., specimens that had not been exposed to a pre-oxidation thermal treatment) in the molten $CaCl_2$-NaCl salt in air at 750°C. Plots of the as-polished Ni specimen mass change per area, Δm/A, as a function of immersion time in this molten salt are shown in **Figures 3.2-2a** and **c**. Unlike the pre-oxidized (NiO/Ni) specimens, these Ni specimens exhibited a significant mass loss with immersion time. The mass loss per area with time was found to exhibit a good fit to linear kinetics (**Figure 3.2-2c**), with similar Δm/A values obtained for corrosion of these specimens in molten $CaCl_2$-NaCl salts

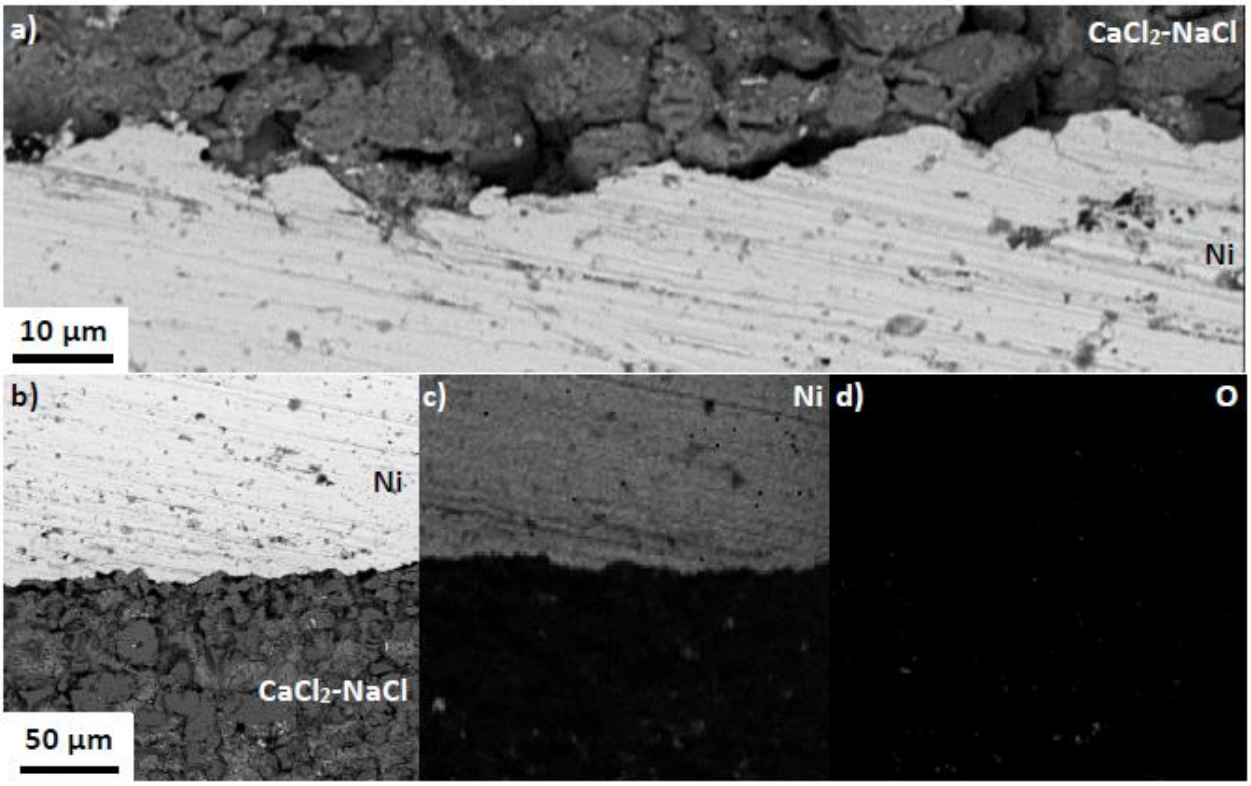

Figure 3.2-4. The interface between a Ni specimen and solidified $CaCl_2$-NaCl liquid: **a)**, **b)** BSE images and **c)**, **d)** associated elemental maps for Ni and O, respectively, obtained from a polished cross-section of an as-polished Ni sample that had been exposed to a $CaCl_2$(53 mol%)-NaCl liquid for 48 h in ambient air at 750°C

without and with presaturation with NiO. Backscattered electron (BSE) images, and elemental maps (from EDX analyses), of a polished cross-section of the interface between a Ni specimen and solidified $CaCl_2$-NaCl salt, after exposure of the specimen to the molten salt for 48 h in air at 750°C, are shown in **Figure 3.2-4**. A continuous NiO layer was not detected at the interface between the Ni specimen and solidified $CaCl_2$-NaCl salt. Although the formation of NiO was thermodynamically favored (as discussed above), the nucleation and growth of a continuous external NiO scale on the Ni surface was apparently kinetically inhibited in the presence of the molten $CaCl_2$-NaCl salt. The resulting direct exposure of the Ni specimens to the molten $CaCl_2$-NaCl salt, and the observed specimen mass loss with time, were consistent with the corrosion of Ni via reaction and dissolution into the molten $CaCl_2$-NaCl salt. Indeed, relatively rapid rates of such Ni reaction and dissolution into the molten salt (**Figures 3.2-2a and c**), compared to the rates of NiO nucleation and sideways growth at the Ni/molten salt interface, would inhibit the formation of a continuous NiO scale on the Ni surface.

This work demonstrates that air-stable, $CaCl_2$-NaCl-based liquids may be contained (e.g., in pipes and tanks) within corrosion-resistant materials that possess continuous, external oxide scales that exhibit slow (parabolic) growth kinetics in the salt in air at 750°C (or within containment materials comprised entirely of such oxides). The thermodynamic calculations above indicated that this corrosion-resistant containment concept for air-

stable molten chlorides may be extended, beyond NiO-bearing Ni, to metal alloys capable of forming other slow-growing external oxide scales in air at 750°C, such as Cr_2O_3-bearing or Al_2O_3-bearing alloys (e.g., oxidation-resistant Fe-based or Ni-based alloys) [33,34]. The thermodynamic calculations above also indicated that other multicomponent, air-stable molten chloride salts (beyond just the $CaCl_2$-NaCl salt of the present work) may be utilized for reliable (air-tolerant) heat transfer and TES (i.e., ternary to quintenary salts comprised of $CaCl_2$, $SrCl_2$, $BaCl_2$, NaCl, and/or KCl). For example, lower-melting $CaCl_2$-NaCl-$BaCl_2$ and $CaCl_2$-NaCl-$BaCl_2$-KCl salts (with reported liquidus temperatures of 440-454°C [28,30,35,36] and 421°C [37] respectively) may be utilized.

Task 4.0: Identify Most Acceptable Corrosion Mitigation Conditions

Milestone 4: Identify atmospheric, chemical, and fluid dynamic conditions most acceptable to the CSP industry for achieving projected annual corrosion rates of ≤30 μm/year for metal alloys and ceramic composites in molten chloride salts at targeted temperatures

After the lab reopened from the 3-month COVID19 shutdown, the effort for this project was focused on rotating-disk corrosion experiments with H214 specimens for Subtask 2.1 (Determining Kinetic Mechanisms Controlling Molten Chloride Corrosion at Low-Oxygen Partial Pressures) and on identifying and demonstrating air-stable molten chlorides and corrosion-resistant containment of such chlorides for Subtask 3.2 (Tailoring Corrosion Conditions at High-Oxygen Partial Pressures). Unfortunately, with these priorities, work was not conducted on Task 4.0.

KEY ACCOMPLISHMENTS

The key accomplishments associated with each task are summarized below.

Task 1.0: Develop Corrosion Testing Equipment and Protocols

- A rotating-disk corrosion testing apparatus was successfully designed, constructed and used to evaluate the corrosion kinetics of a metal alloy under forced-convective conditions. This corrosion testing apparatus operated under controlled atmospheres (e.g., with oxygen-gettered UHP Ar at an oxygen partial pressure, pO_2, $\leq 10^{-14}$ atm, or at a high oxygen partial pressure, such as flowing synthetic air), over a range of controlled rotation rates (50 ± 2 to 1000 ± 2 rpm) at 750 ± 5^oC and up to 900^oC (for a fused silica furnace tube) or 1200^oC (for a mullite furnace tube).
- The rotating-disk corrosion testing apparatus was successfully used to evaluate the corrosion behavior (via mass change measurements) of a Haynes 214 (H214, a Ni-Cr-Al-Fe-Co-based) alloy under conditions of laminar flow with a semi-infinite molten salt bath. **Milestone 1** *(Demonstrate the capability of measuring corrosion kinetics in molten salts at CSP-relevant temperatures under well-controlled thermal, atmospheric, and fluid dynamic conditions)* **was accomplished.**

Task 2.0: Determine Kinetic Mechanisms Controlling Molten Chloride Corrosion

- Rotating-disk corrosion experiments were conducted with H214 alloy specimens in a molten $MgCl_2$-KCl-NaCl (40-40-20 mole%) salt at 50-1000 rpm at 750^oC and in a dry, low-oxygen-bearing ($pO_2 \leq 10^{-14}$ atm) Ar atmosphere. An increase in the specimen rotation rate (or in the square root of the specimen rotation rate) did not result in an apparent increase in the specimen mass change per area. Appreciable scatter was observed in this data, however, which may have been a result of the incomplete and varied coverage of the specimen surfaces with oxide product (Al_2O_3-MgO-bearing) layers. Given such scatter in the data, and the absence of an apparent trend in the mass change/area with specimen rotation rate, liquid phase diffusion could not be confirmed to be a rate-limiting step for the corrosion of H214 in molten $MgCl_2$-KCl-NaCl at 750^oC at low oxygen partial pressures.
- Electron microscopic analyses indicated the presence of a Cr-Al-depleted zone near the molten-salt-exposed surface of the H214 alloy, along with the formation of discontinuous external oxide (Al_2O_3-MgO-bearing) scales, consistent with thermodynamic calculations. The average depletion zone thickness was not found to increase as the specimen rotation rate increased in the $MgCl_2$-KCl-NaCl liquid bath at 750^oC at $pO_2 \leq 10^{-14}$ atm (although appreciable scatter was also observed in this data).
- These kinetic observations were inconsistent with liquid phase as a rate-limiting step for the corrosion of H214 in molten $MgCl_2$-KCl-NaCl under these conditions. **Milestone 2** *(Identify the rate laws and associated mechanism(s) (rate-limiting step(s)) for the corrosion of metallic and ceramic composite specimens in molten chloride salts at CSP-relevant temperatures over a range of atmospheric conditions)* **was partially accomplished.**

Task 3.0: Minimize Corrosion Kinetics

- Thermodynamic calculations were used to identify earth-abundant chloride salts that are more resistant to oxidation in ambient (water vapor-bearing) air at 750°C than $MgCl_2$-bearing salts. The oxidation resistance of one such $MgCl_2$-free salt, a eutectic $CaCl_2$-NaCl composition (53-47 mol%, T_{eut} = 500±8°C [24-28]), in ambient air (with a water vapor partial pressure of $2.3x10^{-3}$ atm) was demonstrated at 750°C via X-ray diffraction analyses and mass change measurements. A eutectic $MgCl_2$-KCl composition (32-68 mol%, T_{eut} = 433±9°C [6,16,17,20-23]) exhibited extensive oxidation, as revealed by MgO formation with appreciable associated weight loss, under similar conditions.
- Pre-oxidized Ni (with a layer of NiO) has been shown to exhibit a slow parabolic weight gain with time when exposed to the eutectic molten $CaCl_2$-NaCl salt in air at 750°C, consistent with solid-state, diffusion-controlled thickening of the NiO scale (at a rate corresponding to an annual Ni recession of 14 µm).
- **Milestone 3** *(Determine the atmospheric, chemical, and fluid dynamic conditions required to achieve projected annual corrosion of ≤30 µm/year for metal alloys and ceramic composites in molten chloride salts at CSP-relevant temperatures)* **was partially accomplished.**

Task 4.0: Identify Most Acceptable Corrosion Mitigation Conditions

- **Milestone 4** *(Identify atmospheric, chemical, and fluid dynamic conditions most acceptable to the CSP industry for achieving projected annual corrosion rates of ≤30 µm/year for metal alloys and ceramic composites in molten chloride salts at targeted temperatures)* **was not accomplished.**

CONCLUSIONS

The current project has demonstrated that:

- a rotating-disk testing apparatus designed and constructed at Purdue University is capable of conducting corrosion experiments in molten chloride salts under well-controlled thermal, atmospheric, and fluid dynamic (laminar flow, semi-infinite liquid bath) conditions (e.g., in a $MgCl_2$-KCl-NaCl/40-40-20 mole% salt at 750^{o}C at an oxygen partial pressure $\leq 10^{-14}$ atm at 50-1000 rpm)
- exposure of a Haynes 214 (H214) alloy to a $MgCl_2$-KCl-NaCl (40-40-20 mole%) salt at 750^{o}C at an oxygen partial pressure $\leq 10^{-14}$ atm resulted in the formation of surface oxide (Al_2O_3-MgO-bearing) product layers and a Cr-Al-depleted zone near the alloy surface (consistent with thermodynamic calculations)
- an increase in the H214 specimen rotation rate (or in the square root of the specimen rotation rate) in the molten $MgCl_2$-KCl-NaCl salt at 750^{o}C at $pO_2 \leq 10^{-14}$ atm:
  - did not result in an apparent increase in the specimen mass change per area, and
  - did not result in an apparent increase in the depletion zone thickness near the alloy surface

  which were inconsistent with liquid-phase diffusion as a rate-limiting step for H214 corrosion, although appreciable scatter was observed for both kinetic data sets (which may have resulted from the incomplete and varied coverage of H214 specimen surfaces with the oxide product, Al_2O_3-MgO-bearing, layers)
- a molten eutectic $CaCl_2$-NaCl (53-47 mole%) salt is resistant to oxidation in ambient (water-vapor-bearing) air at 750^{o}C, whereas a molten eutectic $MgCl_2$-KCl (32-68 mole%) salt exhibited appreciable oxidation under similar conditions (consistent with thermodynamic calculations)
- NiO-bearing Ni is resistant to corrosion in the molten eutectic $CaCl_2$-NaCl salt at 750^{o}C in air, with such corrosion occurring at a slow parabolic rate (consistent with solid-state diffusion through NiO as the rate-limiting step) corresponding to an annual Ni recession of 14 µm

PATH FORWARD

While the results of this project are promising, further work is needed in the following areas.

- The choice of robust, oxidation-resistant, earth-abundant molten salt compositions for reliable heat transfer or thermal energy storage may be extended beyond the binary eutectic $CaCl_2$-NaCl molten salt of the present work to include a wide variety of ternary to quintenary molten chlorides comprised of $CaCl_2$, $SrCl_2$, $BaCl_2$, NaCl, and/or KCl that can be selected for tailored properties (such as reduced liquidus temperatures, relative to the eutectic $CaCl_2$-NaCl liquid). The thermal and chemical properties of such air-stable salts should be evaluated in order to model and predict that behavior of these robust salts as media for high-temperature heat transfer and thermal energy storage.

- Thermodynamic calculations indicate that the containment of such air-stable molten chlorides may be extended beyond NiO-bearing Ni to metal alloys capable of forming other slow-growing external oxide scales in air at 750°C, such as Fe-based or Ni-based alloys capable of forming continuous, external Cr_2O_3-based or Al_2O_3-based scales. Further work is needed to evaluate the corrosion behavior of such Cr_2O_3-forming and Al_2O_3-forming structural metal alloys in air-stable molten chlorides at $\geq$750°C at high oxygen partial pressures under well-controlled fluid dynamic conditions, such as can be conducted with the rotating-disk corrosion-testing apparatus designed and constructed at Purdue University.

INVENTIONS, PATENTS, PUBLICATIONS AND OTHER RESULTS

Patent Applications

1. Kenneth H. Sandhage, “Heat Transfer/Storage Fluids and Systems that Utilize Such Fluids,” *U.S. Patent Application* 15/931982, 2020 (*U.S. Provisional Patent Application* 62/847881, 2019)

Journal Articles

1. Adam S. Caldwell, Grigorios Itskos, Kenneth H. Sandhage, “Air-Stable, Earth-Abundant Molten Chlorides and Corrosion-Resistant Containment for Chemically-Robust, High-Temperature Thermal Energy Storage for Concentrated Solar Power,” *Materials Today*, in press (2021); https://doi.org/10.1016/j.mattod.2021.02.015

Conference Presentations

1. Adam S. Caldwell, Grigorios Itskos, Saeed Bagherzadeh, Mario R. Caccia, Kenneth H. Sandhage, "High-Temperature, Air-Compatible Molten Salts, and an Associated Corrosion-Resistant Containment Strategy, for Cost-Effective, Reliable Heat Transfer and Thermal Energy Storage", TMS 2021, March 2021 (poster presentation)
2. Adam S. Caldwell, Grigorios Itskos, and Kenneth H. Sandhage, "Air Stable Molten Salts and Corrosion Resistant Containment for High-Temperature Thermal Energy Storage and Heat Transfer for Concentrated Solar Power", MS&T 2020, Nov. 2020 (online conference)
3. Adam S. Caldwell, Grigorios Itskos, and Kenneth H. Sandhage, "Air-Stable Molten Salts and Corrosion-Resistant Containment for High-Temperature Thermal Energy Storage", SolarPACES 2020, Oct. 2020 (online conference)

REFERENCES

1. S. Pfenninger, P. Gauché, J. Lilliestam, K. Damerau, F. Wagner, A. Patt, “Potential for Concentrating Solar Power to Provide Baseload and Dispatchable Power,” *Nat. Clim. Change*, **4**, 689–692 (2014).
2. P. Denholm, M. Mehos, ”Enabling Greater Penetration of Solar Power Via the Use of CSP with Thermal Energy Storage,” *Technical Report NREL/TP-6A20-52978*, National Renewable Energy Laboratory, Golden, CO, USA, 2011.
3. P. Denholm, H. Maureen, “Grid Flexibility and Storage Required to Achieve Very High Penetration of Variable Renewable Electricity,” *Energy Pol.*, **39**, 1817–1830 (2011).
4. L. A. Weinstein, J. Loomis, B. Bhatia, D. M. Bierman, E. N. Wang, G. Chen, “Concentrating Solar Power,” *Chem. Rev.*, **115**, 12797-12838 (2015).
5. G. Mohan, M. B. Venkataraman, J. Coventry, “Sensible Energy Storage Options for Concentrating Solar Power Plants Operating Above 600^{o}C,” *Renew. Sustain. Energy Rev.*, **107**, 319-337 (2019).
6. X. Xu, G. Dehghani, J. Ning, P. Li. Basic, “Properties of Eutectic Chloride Salts NaCl-KCl-$ZnCl_2$ and NaCl-KCl-$MgCl_2$ as HTSs and Thermal Storage Media Measured Using Simultaneous DSC-TGA,” *Sol. Energy*, **162,** 431-441 (2018).
7. P. D. Myers Jr., D. Y. Goswami, “Thermal Energy Storage Using Chloride Salts and Their Eutectics,” *Appl. Therm. Eng.*, **109**, 889-900 (2016).
8. W. Ding, H. Shi, Y. Xiu, A. Bonk, A. Weisenburger, A. Jianu, T. Bauer, “Hot Corrosion Behavior of Commercial Alloys in Thermal Energy Storage Material of Molten $MgCl_2$/KCl/NaCl Under Inert Atmosphere,” *Sol. Energy Mater. Sol. Cells*, **184**, 22-30 (2018).
9. W. Ding, A. Bonk, T. Bauer, “Corrosion Behavior of Metallic Alloys in Molten Chloride Salts for Thermal Energy Storage in Concentrated Solar Power Plants: A Review,” *Front. Chem. Sci. Eng.***, 12**, 564-576 (2018).
10. K. Vignarooban, X. Xu, A. Arvay, K. Hsu, A. M. Kannan, “Heat Transfer Fluids for Concentrating Solar Power Systems – A Review,” *Appl. Energy*, **146**, 383–396 (2015).
11. T. Bauer, N. Pfleger, N. Breidenbach, M. Eck, D. Laing, S. Kaesche, “Material Aspects of Solar Salt for Sensible Heat Storage,” *Appl. Energy*, **111**, 1114-1119 (2013).
12. A. R. Cooper, “Modification of Noyes - Nernst Equation,” *J. Chem. Phys.*, **83**, 284 (1962).
13. B. Y. B. Levich, “The Theory of Concentration Polarisation,” *Discuss. Faraday Soc.*, **1**, 37-49 (1947).
14. E. C. Cobb, O. A. Saunders, “Heat Transfer From a Rotating Disk,” *Proc. Royal Soc.*, **236**, 343–51 (1955).

15. Y. Li, X. Xu, X. Wang, P. Li, Q. Hao, B. Xiao, “Survey and Evaluation of Equations for Thermophysical Properties of Binary/Ternary Eutectic Salts from NaCl, KCl, $MgCl_2$, $CaCl_2$, $ZnCl_2$ for Heat Transfer and Thermal Storage Fluids in CSP,” *Sol. Energy*, **152**, 57–79 (2017).
16. I. Barin, *Thermochemical Data of Pure Substances*, 3rd Edition, VCH Verlagsgesellschaft mbH, 1995
17. K. V. Gourishankar, M. Kraminezhad Ranjbar, G. R. St. Pierre, “Revision of the Enthalpies and Gibbs Energies of Formation of Calcium Oxide and Magnesium Oxide,” *J. Phase Equil.*, **14** (5), 601-611 (1993).
18. P. Chartrand, A. D. Pelton, “Thermodynamic Evaluation and Optimization of the LiCl-NaCl-KCl-RbCl-CsCl-$MgCl_2$-$CaCl_2$ System Using the Modified Quasi-Chemical Model,” *Metall. Mater. Trans. A*, **32 A**, 1361-1383 (2001).
19. J. J. Egan, J. Bracker, “Thermodynamic Properties of Some Binary Fused Chloride Mixtures Obtained from E.M.F. Measurements,” *J. Chem. Thermodynamics*, **6**, 9-16 (1974).
20. G. S. Perry, H. Fletcher, “The Magnesium Chloride-Potassium Chloride Phase Diagram,” *J. Phase Equil.*, **14**, 172-178 (1993).
21. K. Grjotheim, J. L. Holm, M. Roetnes, “Phase Diagrams of the Systems Sodium Chloride-Magnesium Chloride and Potassium Chloride-Magnesium Chloride,” *Acta Chem. Scand.,* **26**, 3802-3803 (1972).
22. W. Klemm, K. Beyersdorfer, J. Oryschkewitsch, “Binary Systems of Halides. II. The Behavior of Sodium, Potassium, Rubidium Chlorides and Sodium and Potassium Iodides Toward the Corresponding Magnesium Halides,” *Z. Anorg. Allgem. Chem.*, **256**, 25-36 (1948).
23. G. A. Abramov, “The Ternary System KCl-$MgCl_2$-NaCl,” *Metallurg (Leningrad)*, **10**, 82-105 (1935).
24. K. Igarashi, H. Ohtani, J. Mochinaga, “Phase Diagrams of the System $LaCl_3$-$CaCl_2$-NaCl,” *Z. Naturforsh.*, **42a**, 1421-1424 (1987).
25. M. P. Borovkova, A. I. Orekhova, K. A. Aleksandrov, T. A. Puzanova, “Study of the Calcium Chloride-Sodium Chloride System,” *Izv. Vyssh. Uchebn. Zaved., Tsvetn. Metall.*, **4**, 56-9 (1986).
26. T. Hattori, H. Ikezawa, R. Hirano, J. Mochinaga, “Phase Diagram of Ternary Praseodymium Chloride-Calcium Chloride-Sodium Chloride System,” *J. Chem. Soc. Japan*, **6**, 952-955 (1982).
27. A. Seltveit, H. Flood, “Determination of the Solidus Curve by a Tracer Technique. The System $CaCl_2$-NaCl,” *Acta Chem. Scand.*, **12**,1030-1041 (1958).
28. G. Bergman, S. P. Pavlenko, “Composition Diagram of the System NaCl-$CaCl_2$-$BaCl_2$,” *Dokl. Akad. Nauk SSSR*, **27**, 972-973 (1940).

29. P. Chartrand, A. D. Pelton, “Thermodynamic Evaluation and Optimization of the LiCl-NaCl-KCl-RbCl-CsCl-$MgCl_2$-$CaCl_2$-$SrCl_2$ System Using the Modified Quasichemical Model,” *Can. Metall. Quart.*, **39**, 405-420 (2000).

30. P. Chartrand, A. D. Pelton, “Thermodynamic Evaluation and Optimization of the LiCl-NaCl-KCl-RbCl-CsCl-$MgCl_2$-$CaCl_2$-$SrCl_2$-$BaCl_2$ System Using the Modified Quasichemical Method,” *Can. Metall. Quart.*, **41**, 13-32 (2000).

31. JCPDS International Center for Diffraction Data File 00-024-0223 for CaCl2, 00-037-1497 for CaO, 00-044-1481 for $Ca(OH)_2$, 00-041-1475 for $CaCO_3$, 00-041-1476 for KCl, 01-070-1611 for K_2MgCl_4, 01-089-1567 for $MgCl_2$, 00-045-0946 for MgO, 00-005-0628 for NaCl, 00-004-0850 for Ni, 00-047-1049 for NiO, *JCPDS International Center for Diffraction Data*, Newtown Square, PA, USA, 2007.

32. S. Mrowec, Z. Grzesik, “Oxidation of Nickel and Transport Properties of Nickel Oxide,” *J. Phys. Chem. Solids*, **65**, 1651-1657 (2004)

33. K. H. Sandhage, “Heat Transfer/Storage Fluids and Systems That Utilize Such Fluids,” *U.S. Patent Application*, No. 15,931,982, 2020.

34. K. H. Sandhage, “Methods and Materials Systems for Enhancing Corrosion Resistance of Solid Materials and Corrosion-Resistant Devices Made Therefrom,” *U.S. Patent Application*, No. 16,494,922, 2018.

35. T.-O. Sato, T.-I. Amano, “An Investigation of Equilibrium Diagrams of Salts for Salt Baths. IV. The Equilibrium Diagram of the Barium Chloride-Calcium Chloride-Sodium Chloride System,” *Kinz. No Kenk.,* **11**, 305-316 (1934).

36. A. F. Alabyshev, M. F. Lantratov, “The Diagram of State of the Systems Sodium Chloride-Calcium Chloride-Barium Chloride,” *Trudy Leningrad. Technol. Inst. Im Leningrad. Soveta,* **12**, 141-151 (1946).

37. N. S. Prodan, “Study of the Fusibility of the Salt Alloy NaCl-KCl-$CaCl_2$-$BaCl_2$,” *Sb. Tr. Leningr. Inst. Inzh. Zheleznodor. Transp,* **229**, 177-188 (1964).